8-1-2009

Investigation of defects formed by ion implantation of H2+ into silicon

Patrick Whiting

Investigation of Defects Formed by Ion Implantation of H_2^+ into Silicon

By: Patrick Whiting

A Thesis Submitted

in Partial Fulfillment

of the Requirements for the Degree of

Master of Science

In

Materials Science and Engineering

Approved By:

Dr. Karl Hirschman, Advisor

Dr. Santosh Kurinec, Committee Member

Dr. Robert Pearson, Committee Member

Dr. Kalathur Santhanam

MATERIALS SCIENCE AND ENGINEERING

COLLEGE OF SCIENCE

ROCHESTER INSTITUTE OF TECHNOLOGY

ROCHESTER, NY

AUGUST 2009

Foreword

Upon completing this thesis and staring at the title page, I realized that there are so many people that deserve my thanks for their assistance in this thesis. Firstly, I owe a great debt to Karl Hirschman, my advisor. Without Karl, I'd still be looking for my first co-op and I would have never had a chance to work at Sullivan Park (Corning Incorporated's research facility in Painted Post, New York), which brings me to the second person I want to thank.

Dick Maschmeyer, formerly of Corning, Inc. (now retired) has likely been the biggest influence on my professional development to date. On my first day of work, during lunch if I remember correctly, I mentioned to Dick that I was interested in learning thermodynamics. Dick launched into an impassioned speech about what a great subject it was and I found what would become my three favorite textbooks on my desk the day after which Dick lent to me for the summer. Without Dick's help, I doubt that I'd have learned the thermodynamics and kinetics necessary for the work I did in this thesis. So, it's not an embellishment to say that if it weren't for Dick, this thesis wouldn't have even been undertaken.

Third, fourth and fifth on the list are Johannes Moll, Greg Couillard and Jayantha Senawiratne, all of Corning, Incorporated. Johannes acted as my supervisor during the period while I was developing the small signal model for DLTS analysis of MIS Capacitors and was the guy I went to when I had ideas or simply wanted a break to talk. Greg acted as secondary advisor to me as my work slowly started to move away from theory and towards experimentation. He was my primary source for materials and for guidance on my experiments (as well as my unofficial mailbox at Corning – thanks dude). Over the past year, I don't think I've gotten more than a half-dozen emails from him that didn't include the phrase, "If there's anything you need from me, let me know". Jayantha was my source for DLTS. If it weren't for his taking the time to run my samples and collaborate on baseline experiments – often coming in on a weekend to run experiments, my DLTS work would have never been completed.

Guys, this thesis is as much a testament to your own hard work, dedication and brilliance as it is to my own hard work. I owe you all a huge debt. Thank you.

Abstract

Ion cutting achieved by the implantation of hydrogen or the co-implantation of hydrogen and helium is among the most common methods for the formation of Silicon on Insulator (SOI) structures used in the semiconductor industry. In this method, hydrogen is implanted into silicon at a high fluence and is heated in order to induce an exfoliation event. During this exfoliation event, a silicon wafer is cleaved along the depth at which the maximum damage concentration occurs, and the cleaved material bonds chemically to any underlying material being used as a handle substrate. The ion implantation process induces a variety of defect species which evolve as they are annealed at varying temperatures and times and the characteristics of these defects and the reactions which dominate their formation are critical for low temperature substrates such as LCD glass.

This study observes the annealing characteristics of a variety of structural and electronic defects induced by ion implantation, including hydrogen decorated monovacancies and hydrogen decorated interstitials. The states arising from these decorated point defects were analyzed using Multiple Internal Transmission Infrared Spectroscopy (MIT-IR) and Deep Level Transient Spectroscopy (DLTS). A method for observing implant-related defects on a MOS Capacitor using a DLTS measurement was developed. A new method for extracting the activation energy and the capture cross section of states observed with DLTS through the use of the Full Width at "N^{th}" Maximum was also developed. MIT-IR spectra resulting from ion implantation were analyzed using a novel method to extract the activation energy, reaction velocity and order of a solid state reaction, termed Kinetic Differential Analysis.

Analysis using the methods described above allowed for the identification of five trap energy levels associated with hydrogen ion implantation which were tentatively assigned to VH_2 (.15eV) VH_3 (~.54eV) and IH_x (.16eV and .19eV) defects. Kinetic Differential Analysis of MIT-IR spectra has identified reaction pathways associated with the "decay" of decorated monovacancy defects These chemical reactions have kinetic reaction orders of approximately 1.5, indicating a secondary reaction which contributes to the decay as well as some general interaction between reactants during the decay process.

Table of Contents

List of Figures

List of Tables

Chapter 1: Introduction

1.1: Motivation

The continuing drive for high performance Complementary Metal Oxide Silicon (CMOS) Transistors has driven material constraints for Silicon substrates to the requirement of Silicon on Insulator (SOI) structures. These structures consist of a thin layer of Silicon on top of a much larger insulating substrate. This substrate may be an insulating crystal, as is the case in Silicon on Sapphire materials, where Silicon is grown epitaxially on top of a Sapphire substrate. Alternatively, the substrate may be formed from a Silicon wafer that is oxidized to form a thin insulating layer [1]. A third option which is far less prevalent than the use of an oxidized substrate is the use of an amorphous insulating material such as glass. This last option is particularly useful for electronics applications where a relatively transparent substrate is required, as is the case for display electronics.

In the case of structure formation on an oxidized crystal or an amorphous substrate, the method for joining the semiconducting layer to the insulating substrate is a bonding technique. Typically, this is accomplished by joining a Silicon wafer to the insulating substrate at room temperature. Van Der Waal's forces generate a weak bond which holds the two substrates together prior to a thermal treatment. This thermal treatment induces much stronger chemical bonding between the insulator (which is typically SiO_2) and the silicon substrate. This bonding technique results in a thick semiconductor substrate bonded to a thick insulating substrate which, alone, is not an improvement over conventional bulk semiconductors.

The semiconductor layer must be thinned down. A thin layer may be formed by lapping and chemical etching of the thick semiconductor layer until the desired thickness is achieved.

Another commonly favored technique is the use of an etch-back, where the semiconducting layer is exposed to an RF plasma and a deep reactive ion etch is performed until the desired thickness is achieved. Both lapping and etch-back techniques are inefficient, at best, because they effectively waste an entire wafer to form an SOI substrate. They are also inherently slow processes because of the time required to etch through or polish down samples which may be a half-millimeter thick or more, as is typically the case for silicon wafers.

Another option which has gained popularity recently is an Ion-Cutting technique [1]. Prior to bonding, the semiconductor substrate goes through an Ion Implantation step, where Hydrogen or a combination of Hydrogen and Helium is implanted into the semiconductor. This gives rise to primary implant-related defects such as self-interstitials and vacancies as well as some hydrogen-defect complexes. Following this ion implantation step, the normal bonding procedure is followed, but the temperature is raised after the bonding process is complete. When exposed to higher temperatures, hydrogen-defect complexes will grow and agglomerate, forming a series of hydrogen-terminated dislocation loops and stacking faults, called blisters. As annealing progresses, hydrogen and helium will coalesce at these blister sites and the rising gas pressure due to higher concentrations within the blisters as well as rising temperature will cause a fracture event which will cleave the wafer. The depth at which fracture and cleaving occurs is the depth into the implanted semiconductor sample where the number of recoils and corresponding number of induced vacancies are maximized [1].

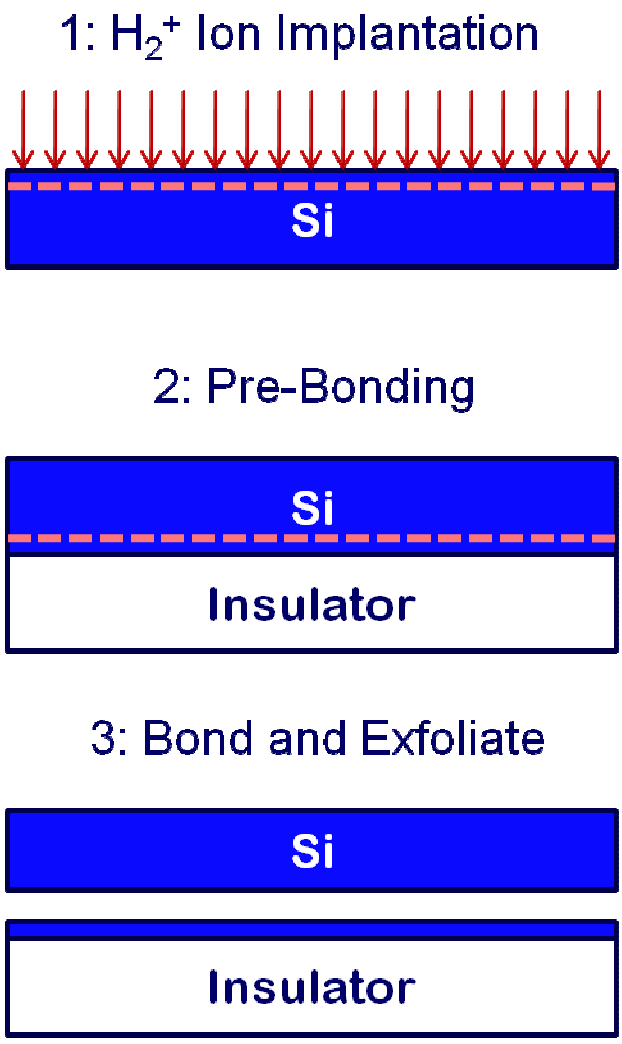

Figure 1: The Hydrogen Ion Cutting Technique – Hydrogen or Hydrogen-Helium is injected into the semiconductor via ion implantation (1). The semiconductor is placed on an insulating substrate, implanted side down (2). The semiconductor substrate is annealed at elevated temperatures, inducing chemical bonding of the semiconductor to the insulator and exfoliating the implanted layer (3).

In all SOI techniques that utilize bonding for sample formation, a critical factor which constrains the effective temperature ceiling for processing after sample formation is the thermal expansion coefficient mismatch between the various thin film layers of the sample. In the case of SOI where silicon is bonded to an oxidized wafer, this is not a significant concern. The thin oxide intermediary between the two silicon layers cannot generate enough stress to induce de-

lamination of the semiconductor film. Thus, lapped, RIE and Ion-Cut SOI created on an oxidized silicon substrate can typically be annealed up to temperatures typical for bulk semiconductor processing. In the case of a sample formed where the substrate is an amorphous material, this mismatch of the thermal expansion coefficient can lead to de-lamination at elevated temperatures, so the ceiling for processing temperature is much lower [1].

Because of the reduced tolerance for high temperatures, samples formed by Ion-Cutting on an amorphous substrate may not be annealed so as to completely eliminate all defects within the sample. Many of the point defects and hydrogen-defect complexes formed during the exfoliation event may remain present within the sample created even after a thermal treatment at the available (albeit low) maximum temperature [2]. These defects lead to degraded device performance primarily through recombination effects. Specifically, the defects formed during implantation which react and form secondary defects after annealing, act as centers for Shockley Read Hall (SRH) Recombination events [3]. Depending upon the characteristics of the trap generated, these centers may act as pseudo-dopants, which can drastically affect the resistivity of the thin film silicon layer or may, alternatively, act as sources of leakage at metallurgical junctions. This second situation results in an increase in the off-state current of devices fabricated on SOI structures, forcing circuit designers to work around higher power consumption on-substrate as well as possibly design far more complex circuits to account for the poor switching quality of their devices.

If commercial products formed from Ion-Cut processes with amorphous insulators are to be inexpensive and ultimately successful, it is imperative that the defects caused by Ion-Cut processes be identified and controlled. To this end, this thesis will seek to identify electrical defects caused by the Ion-Cut process, correlate these defects with associated abnormalities in

crystal structure and propose a means for understanding the reactions that contribute to the formation and dissolution of these defects during the annealing process. This thesis will make use of Deep Level Transient Spectroscopy, a technique developed by D.V. Lang in 1974 [4] as well as Multiple Internal Transmission Infrared (MIT-IR) Spectroscopy [5].

If the effects of structural defects associated with ion cutting techniques are to be correlated with electronic trapping effects, several other technical issues must be worked out in advance. Firstly, an effective method must be found which can relate the annealing dynamics of structural defects to the corresponding annealing dynamics of electronic defects in order to make positive correlations between the two. To this end, finding a repeatable method of forming a sample which can generate a DLTS signal with minimal noise is of the utmost importance. This method must allow for the sample to be implanted with hydrogen and annealed for only "low" temperatures in the range of 300°C to 600°C or, preferably, not annealed at all. The method of formation explored in this text will be a Metal-Insulator-Semiconductor (MOS) Capacitor.

Additionally, a method for analysis of DLTS signals past the typical methodology associated with DLTS is required in order to extract the most data from all measurements. This new method of analysis will likely require the definition of a theoretical function representing a DLTS signal and many of the non-idealities encountered when modeling a DLTS peak with a simplistic model. This new method may also require new empirical analysis methods in order to analyze DLTS spectra in a more efficient, accurate fashion.

1.2: Shockley Read Hall (SRH) Recombination

Shockley Read Hall (SRH) Recombination is a four-pathway kinetic process for charge trapping due to recombination centers existing in a semiconductor [6]. These recombination centers are caused by imperfections within the semiconductor crystal, such as those caused by Ion Implantation. Unlike direct methods of recombination, where electron-hole pairs are eliminated, producing a photon of energy equal to the combined energy lost by the two carriers, SRH Recombination is an indirect process. Electrons and Holes recombine by means of momentum loss in an inelastic collision at a trap center. The energy dissipated in this recombination event may be given off as a lattice vibration, or phonon, which propagates from the trap through the crystal.

In SRH Recombination, the four kinetic pathways which exist may be derived from the behavior of lattice imperfections in the presence of charged particles. Most lattice imperfections may be modeled as single-charged defects. That is, they may exist either as a neutral species or as an ionized species. This behavior is similar to that of dopant atoms which are recombination centers with very shallow ionization energies. Ionization or neutralization may be achieved in two ways. A charge may be gained or may be lost. A defect which ionizes to form a positive (negative) charge may either lose an electron (hole) or gain a hole (electron) to become ionized. To neutralize, this defect must lose a hole (electron) or gain an electron (hole). The act of gaining a charge is referred to as a capture event. The act of losing a charge is referred to as emission. More complex ionization cascades do exist where a defect may have more than one charged state. However, these cascades are rare and analysis is complex in comparison to the relatively simplistic SRH kinetics. Typically, defects which exhibit these cascades are treated as

"close enough" to a single-ionization defect to be analyzed using typical SRH Recombination statistics, particularly at cryogenic temperatures.

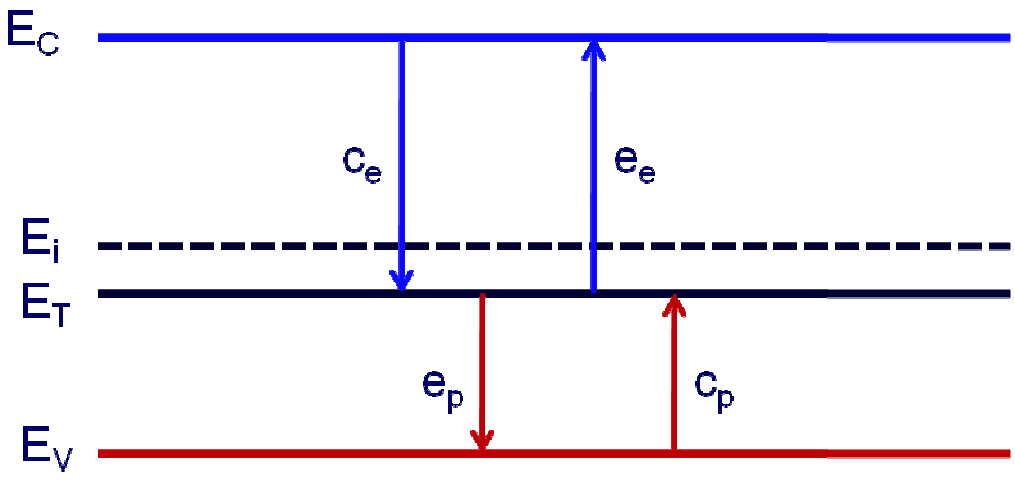

Figure 2: A diagram of Shockley Read Hall (SRH) Recombination for a hole trap center - Electrons may be captured (c_e) from or emitted (e_e) to the conduction band. Holes may be captured (c_p) from or emitted (e_p) to the valence band.

The kinetics of capture and emission are very similar. All defects have some area associated with them which represents their sphere of influence, called a capture cross-section. If a carrier impinges within this area, it will interact with the defect. This constitutes a "collision" between the carrier and the defect. The number of collisions between a carrier and a defect may be defined as the number of instances per unit time where the area swept out by a defect comes into contact with a carrier as the carrier undergoes its "random walk" through the crystal lattice. It stands to reason, therefore, that for a single defect state, the rate of collisions (f_e or f_h) is equal to the thermal velocity (v_e or v_h) and spatial density (n or p) of the carriers multiplied by the capture cross-section (σ_e or σ_h) of the defect state in question. It is important to

note that the spatial density of carriers is, of yet, undefined because the band in question is not yet defined. In the case of capture events, free carriers (holes in the valence band or electrons in the conduction band) are of interest. In the case of emission events, bound carriers (electrons in the valence band or holes in the conduction band) are of interest. The capture cross-section varies based on the carrier type. A defect will have a differently sized area of influence for a hole as compared to an electron.

$$f_e = n\sigma_e v_e \quad (1\text{-}1)$$

$$f_h = n\sigma_h v_h \quad (1\text{-}2)$$

Of the collisions that happen in any given period of time, only a certain number will result in a "reaction" between the carrier and the defect state. The likelihood of this reaction is determined by the statistical quantum mechanics of the reaction which is to take place. In the case of carrier capture, the probability of a reaction occurring during a collision is effectively unity because carriers fall into a potential well. These carriers must be free to move about the crystal, so the density of carriers which is of interest for capture kinetics is the density of free carriers, commonly referred to as n for electrons and p for holes. The carrier capture kinetics are as follows.

$$c_e = n\sigma_e v_e \quad (2\text{-}1)$$

$$c_h = n\sigma_h v_h \quad (2\text{-}2)$$

This is not the case for emission events. During an emission event, carriers are able to overcome the confines of a potential well and are made free to move about the crystal lattice. This effect implies a thermalization event which must be regulated by some statistical mechanical distribution which is dependent upon the depth of the potential well as well as the temperature at which the semiconductor exists. Because when one carrier is emitted, it leaves behind a carrier of the opposite type, the emission of a carrier from a trap state to a given band may be viewed as the capture of an opposite trap state from the same band. So, the emission of an electron (hole) to the conduction (valence) band corresponds to the capture of a hole (electron) from the conduction (valence) band. The density of opposite carriers within the band associated with emission determines the density which is used determine to the rate at which emission occurs. It is assumed that both carrier types have the same density within a given band. Thus, the density of minority carriers within a given band, be it the conduction or valence band is the same as the density of majority carriers within that same band. The resulting equation for emission is as follows, where P(e) or P(h) are the probability functions associated with the emission event, N_C is the density of states in the conduction band and N_V is the density of states in the valence band.

$$e_e = N_C \sigma_e v_e P(e) \quad (3\text{-}1)$$

$$e_h = N_V \sigma_h v_h P(h) \quad (3\text{-}2)$$

Typically, carrier and trap densities are low within a semiconductor and classical Boltzmann Statistics may be applied to the emission probability. The trap level is assumed to be the ground potential in this case, with the energy of the barrier equal to the difference in energy between the band to which the emission is occurring and the trap energy. The result is the final expression for hole and electron emission probability, where E_T is the trap energy, E_C is the conduction band edge energy, E_V is the valence band edge energy, k is Boltzmann's Constant and T is the temperature of the semiconductor in Kelvins. The difference between E_T and E_C or E_V may also be expressed as equal to an activation energy, ΔE.

$$e_e = N_C \sigma_e v_e \exp\left[(E_T - E_C)/kT\right] \quad (4\text{-}1)$$

$$e_h = N_V \sigma_h v_h \exp\left[(E_V - E_T)/kT\right] \quad (4\text{-}2)$$

Given the constraints on SRH kinetics listed above, the differential equations defining the transient characteristics of hole-filled and electron-filled trapping states may be described as follows where the variable t is the time associated with the transient process. It is important to note that these terms describe the kinetics of formation assuming a concentration of trap states equal to unity.

$$\frac{dp_T}{dt} = n_T(e_n + c_p) - p_T(e_p + c_n) \quad (5\text{-}1)$$

$$\frac{dn_T}{dt} = -n_T(e_n + c_p) + p_T(e_p + c_n) \quad (5\text{-}2)$$

In order to determine the true rates and the true transient concentration of trap states, the rates above and their associated concentrations must be multiplied by the true concentration of trapping states. For the sake of simplicity, we redefine the preceding differential equations as follows, assuming that any trap which is not filled with a hole must be filled with an electron.

$$\frac{dp_T}{dt} = (K_n) - p_T(K_p + K_n) \quad (6\text{-}1)$$

$$\frac{dn_T}{dt} = (K_p) - n_T(K_n + K_p) \quad (6\text{-}2)$$

In the simplest case of SRH Recombination, only two charge states are permitted for a single defect structure, a neutral state and a positively or negatively charged state. In some cases, most notably for vacancies in semiconductors, it is possible for multiple charge states to exist past the neutral state. These cases represent dynamics which require far more complex analysis and will not be treated in this text.

1.3: Deep Level Transient Spectroscopy (DLTS)

Deep Level Transient Spectroscopy (DLTS) began as a differential capacitive technique developed by D.V. Lang in 1974 [4] and has since extended to a variety of other differential charge sensing methods, including Charge Transient Spectroscopy (QTS), Constant Capacitance

Deep Level Transient Spectroscopy (CCDLTS), Current Transient Spectroscopy (CTS) and Photo-Induced Transient Spectroscopy (PITS). These various sensing methods may be applied to a large variety of devices including Schottky Diodes, PN Junction Diodes, MOS Capacitors, MOS Transistors, Bipolar Junction Transistors and so on. The methodology common to these techniques is the observation of charge decay in a semiconductor at cryogenic temperatures.

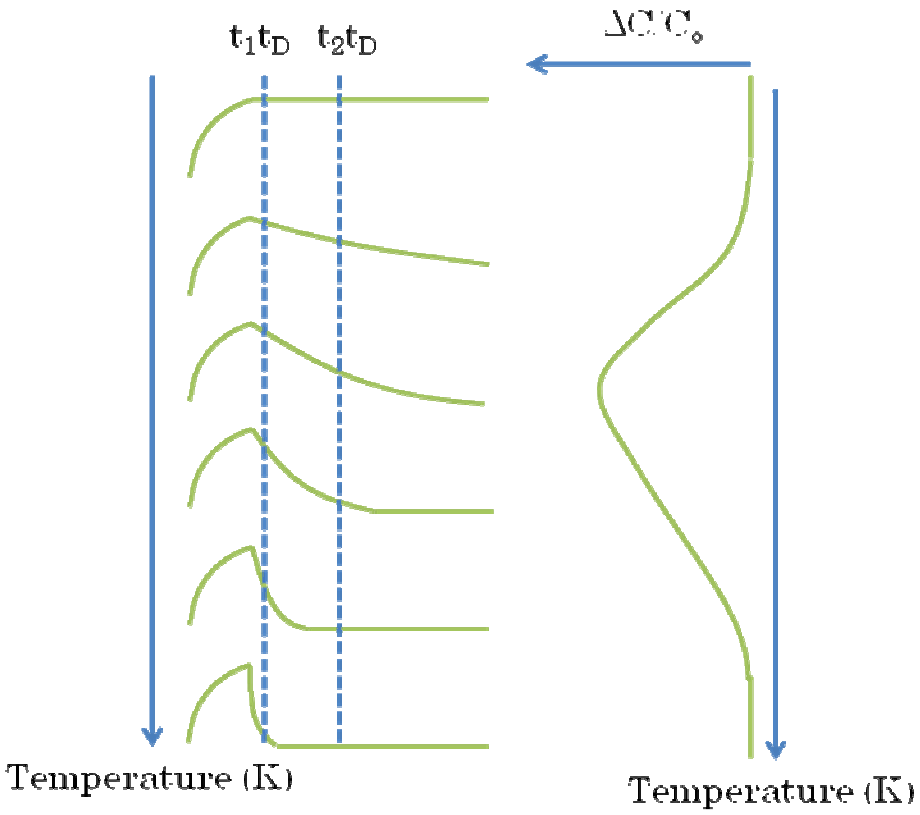

Figure 3: Generation of a Deep Level Transient Spectroscopy signal. This is achieved by monitoring the variation in the change in the decaying normalized capacitance ($\Delta C/C_O$) defined by the discrete differential with respect to time sampled at two separate times, t_1t_D and t_2t_D (where t_1 and t_2 are constants and t_D is the "time delay").

This signal can be sinusoidal, as in the case of a lock-in technique, or a square wave of variable duty cycle, as is the case in a boxcar differentiation technique. During boxcar

differentiation, the signal is designed to bias the structure in such a way that traps fill during a short "filling" pulse (labeled hereafter as t_f) and then emit when the signal transitions to a much longer "emission" pulse (hereafter labeled t_e). For the purposes of modeling, this emission pulse may be assumed to be infinite.

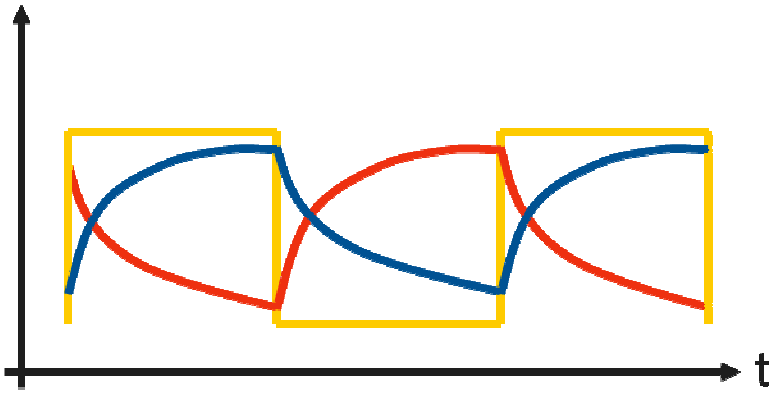

Figure 4: The potential settings (yellow), majority carrier trap (red) and minority carrier (blue) trapping probabilities for a generic DLTS transient.

Measurement of the charge transient occurs during the emission pulse, as it is typically dominated by thermalization of carriers from filled trap states. Boxcar differentiation is achieved by measuring the charge levels present within the semiconductor at two separate points, t_1 and t_2, in order to derive an expression for the discrete differential charge. In this situation, the filling pulse acts as a means of defining the initial concentration of trapped charge, the transient of which is observed during the emission pulse.

With these constraints in mind, we may derive an expression for the observable decay in filled trap states over time. We observe in equations (7) and (8) that the differential

corresponding to this decay is a linear 1st Order Differential Equation and solve it in terms of boundary conditions defined by the filling pulse, p_{T0} and n_{T0}.

$$p_T = \frac{K_n^e}{K_n^e + K_p^e} + p_{T0} e^{[-(K_n^e + K_p^e)t(1,2)]} \quad (7\text{-}1)$$

$$n_T = \frac{K_p^e}{K_n^e + K_p^e} + n_{T0} e^{[-(K_n^e + K_p^e)t(1,2)]} \quad (7\text{-}2)$$

The equilibrium condition attained as the measurement time is allowed to proceed to infinity is the first term in the sums listed above. The secondary term represents the transient decay of the charge state from the conditions set up by the filling pulse to the equilibrium conditions inherent to the conditions described as part of the emission pulse. Thus, the magnitudes of the transient constants, p_{T0} or n_{T0}, are equal to the difference between the initial trapped charge concentration (defined by the filling pulse) and the final concentration which the emission transient approaches asymptotically as time increases to infinity. These transient constants may be defined as is shown below.

It is important to note that the kinetic rates (K^f and K^e) are defined by the carrier concentration existent during filling and emission pulses and, therefore, have different values during these different pulses.

$$p_{T0} = F_{TP} - \frac{K_n^e}{K_n^e + K_p^e} \quad (8\text{-}1)$$

$$n_{T0} = F_{TN} - \frac{K_p^e}{K_n^e + K_p^e} \quad (8\text{-}2)$$

The terms F_{TP} and F_{TN} are the trapped carrier concentrations achieved at the end of the filling pulse transient (when the transition is made from the filling pulse to the emission pulse). The concentration at the end of the filling pulse may be defined as follows.

$$F_{TP} = \frac{K_n^f}{K_n^f + K_p^f} + A_{TP} e^{[-(K_n^f + K_p^f)t_f]} \quad (9\text{-}1)$$

$$F_{TN} = \frac{K_p^f}{K_n^f + K_p^f} + A_{TN} e^{[-(K_n^f + K_p^f)t_f]} \quad (9\text{-}2)$$

A_{TN} and A_{TP} represent the difference between the trapped charge concentration present at the start of the filling pulse (which is equal to the steady state condition of the emission pulse) and the steady-state trapped charge concentration that would result from an infinite filling pulse.

$$A_{TP} = \left(\frac{K_n^e}{K_n^e + K_p^e} - \frac{K_n^f}{K_n^f + K_p^f} \right) \quad (10\text{-}1)$$

$$A_{TN} = \left(\frac{K_p^e}{K_n^e + K_p^e} - \frac{K_p^f}{K_n^f + K_p^f} \right) \quad (10\text{-}2)$$

With the equations listed above, the transient observed during analysis with DLTS may be fully defined for any time during the emission pulse as well as for any filling pulse width

provided that the emission pulse conditions are existent for a long enough time that the state of the semiconductor may be considered to be in thermal equilibrium.

This charge transient is differentiated, typically by sensing the differential charge at two times during the decay and subtracting the two measurements. Typically, the assumption of complete filling prior to the emission pulse is made and the equation most typically used to define the resulting differential signal from this charge decay is as follows.

$$\Delta p_T = \exp\left(-e_p t_1\right) - \exp\left(-e_p t_2\right) \quad (11\text{-}1)$$

$$\Delta n_T = \exp\left(-e_n t_1\right) - \exp\left(-e_n t_2\right) \quad (11\text{-}2)$$

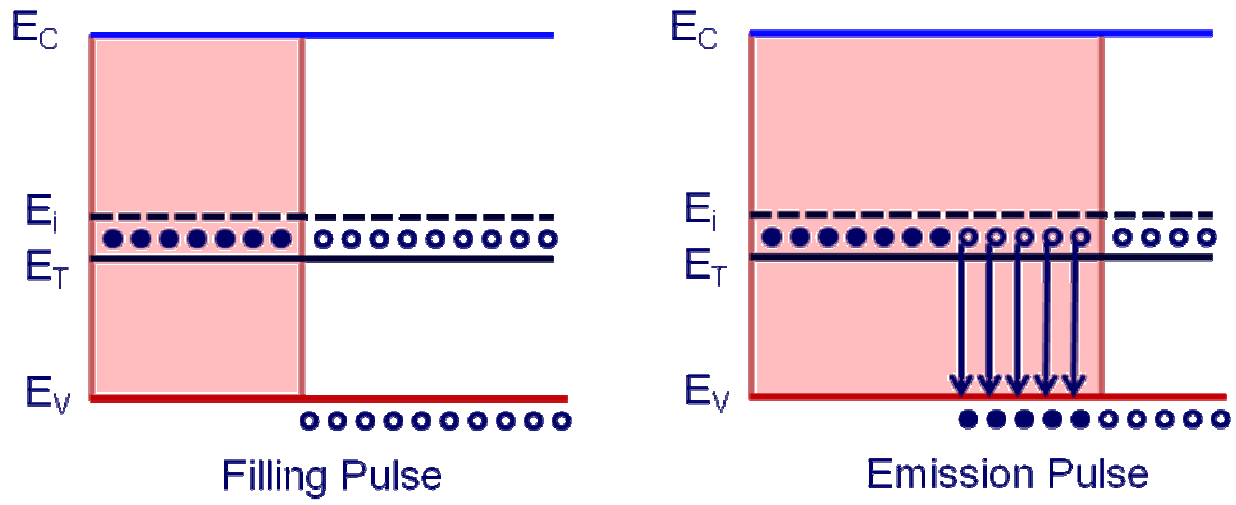

Figure 5: Diagrams of the free carrier behavior of a single-sided junction during the thermal equilibrium induced by the Filling Pulse and during the transient state of non-equilibrium immediately following the application of the Emission Pulse. These diagrams represent the behavior of a hole trap. In an electron trap, trapped carriers would be emitted to the Conduction Band.

A spectrum is created by plotting this differential over a wide range of temperatures (as in Figure 3) with each peak in the spectrum representing a different trap species. By iterating a scan with variable values of t_1 and t_2, a family of spectra may be created. An important metric that defines these spectra is the rate window, τ, which is a function of t_1 and t_2. This rate window corresponds to the inverse emission rate at the peak maximum. It is defined as follows.

$$\tau = t_D[t_1 - t_2]/[\ln^{-1}(t_1/t_2)] \quad (12)$$

The activation energies and capture cross-sections of these trap species can be determined via an Arrhenius Plot of the temperature corresponding to the peak maximum, τ_m. In this Arrhenius Plot, the natural logarithm of $T_m^2\tau_m$ is plotted against $1/kT_m$. The result of this plot is an expression for the difference between the trap energy and the band energy, ΔE, which is represented by the slope of the Arrhenius Plot. The plot also yields the Capture Cross-Section of the trap, which corresponds to the point at which the Arrhenius plot intercepts a value of $1/kT_m$ equal to zero.

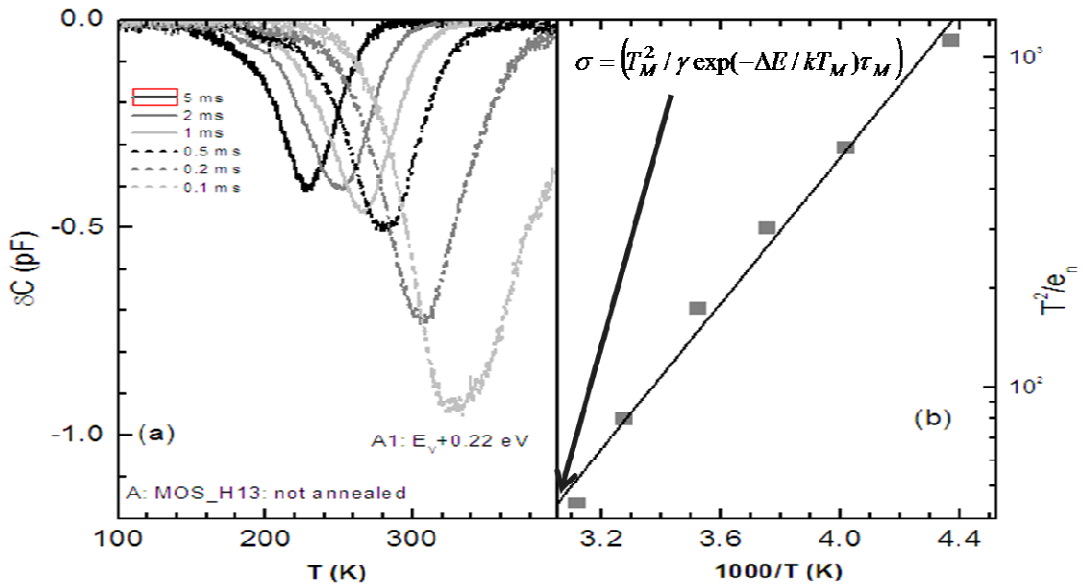

Figure 6: Arrhenius plotting of a signal arising from a single deep level trap observed using Deep Level Transient Spectroscopy. The slope of the derived Arrhenius Plot yields the activation energy of the deep level trap while the point where the deep level trap intercepts the $T^2\tau$ axis yields the capture cross-section. (Courtesy J. Senawiratne of Corning, Incorporated)

A value for the concentration of trap states present within the semiconductor may be derived from the expression for the depletion capacitance of a single-sided junction. It is as follows, where C_o is the capacitance at infinite time, ΔC_M is the change in capacitance observed at the maximum of the DLTS signal, N_T is the trap concentration and N_A is the dopant concentration in the semiconductor.

$$N_T = 2N_A\Delta C_M/C_o \quad (13)$$

1.4: Multiple Internal Transmission Infrared (MIT-IR) Spectroscopy

Multiple Internal Transmission Infrared (MIT-IR) Spectroscopy is a Fourier Transform Infrared (FTIR) Spectroscopy technique which is exceptionally well-suited to the measurement and observation of bonding and structural defects both at material interfaces as well as within bulk materials [5]. MIT-IR couples light generated by an infrared source into a bulk material through the use of a prism with its edges beveled at a precise angle. This prism has a matching refractive index in comparison to the index of the material being observed, often because it is formed from the same material. Because of this, light may be easily coupled into the sample being evaluated after being transmitted into the prism. As this light passes through the sample, it eventually will encounter the back interface between the sample and the ambient and reflect back in the direction of the prism. The prism itself is etched in the center in order to confine the light to the sample until it reaches the other side of the region being probed, at which point the light couples back into the prism and then back out into the ambient. At this point it is sampled by a detector. The intensity of the light reflecting through the sample is dissipated by the reflective losses caused by imperfect reflection at sample interfaces, to transmission loss of incident light flowing into and out of the prism and, most importantly, to absorption of the infrared beam within the sample due to both the sample material itself as well as defects induced by ion implantation within the sample.

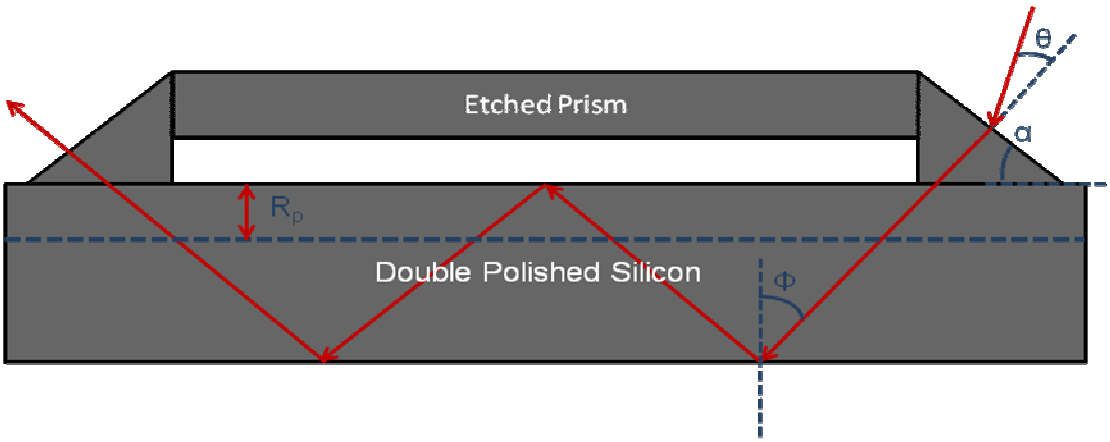

Figure 7: MIT-IR Sample Design – The guided infrared beam strikes the prism at an incident angle, θ. The angle of the prism normal with respect to the sample, α, determines the angle at which the beam strikes the bottom surface of the sample, Φ. R_p defines the extent of the implant damage profile. Transmission into and out of the prism as well as reflections off of each top and bottom surface of the sample contribute to attenuation.

The intensity loss due to each of these components is dependent upon the number of bounces the infrared beam undergoes during its transit through the sample. The effective path-length that the light travels over during its bouncing transit through the sample is determined by the incident angle of the light in comparison to the bevel, the bevel angle in comparison to the surfaces of the prism and the dimensions of the sample and the prism themselves. In order to properly analyze the attenuation experienced by the infrared beam during its transit through the combination of the prism and sample, the effective path-length of the light must be estimated. In order to perform this estimation, the incident angle of the infrared beam in relation to the normal of the beveled edge of the prism, θ, must be known. The angle of the bevel in relation to the bottom surface of the prism, α, must also be known along with the length of the bottom surface of the prism, d, and the thickness of the sample, t. The path that the incident beam takes after passing through the prism bevel may be calculated by making use of Snell's Law with the implicit assumption that the extinction coefficient is much lower in magnitude than the refractive

index. In this derivation, n_V is the refractive index of the ambient enclosing the prism and sample and n_P is the refractive index of the prism and, by association, the refractive index of the sample. By noting that the intersection of the bevel with the incident beam and with the bottom surface of the prism forms a triangle, the following equation may be stated relating the angle of the transmitted beam with the bottom surface of the prism, □ [7].

$$\phi = \alpha - \arcsin\left(\frac{n_V}{n_P}\sin\theta\right) \quad (14)$$

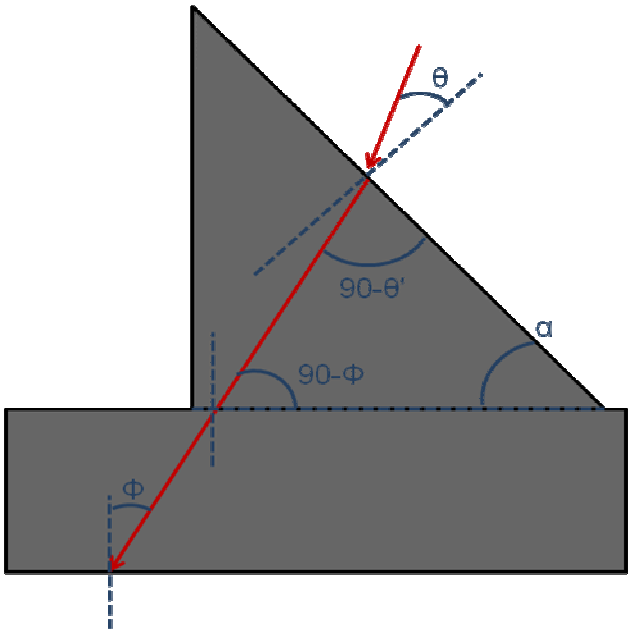

Figure 8: The geometry formed by an infrared beam as it passes through the combination of a prism and sample with similar refractive indices. The path of the infrared beam through the prism and through the interface between the prism and sample defines a triangle and this geometry may be used to calculate Φ.

This angle defines the angle at which the infrared beam bounces off of each horizontal interface on the sample. From the angle, □, the path length may be calculated to a first order by calculating, first, the distance traveled by the infrared beam in the sample during a single bounce and, secondly, calculating the number of bounces that the infrared beam undergoes off of either surface of the sample. The path length per bounce of the infrared beam is simply the thickness of the sample divided by the cosine of the angle. From the assumption that the incident beam enters and leaves the sample at the edges of the prism, the number of bounces, n, may be related to this path length per bounce by considering the horizontal distance traveled per bounce, which is simply the path length of a single bounce multiplied by the sine of the incident angle, □. Dividing the total length of the bottom surface of the prism by this distance traveled for a single bounce yields the following expression for n by virtue of the observation that a bounce off of the bottom surface is a mirror image of a bounce off of the top surface.

$$n = (d/(tan\phi t)) \quad (15)$$

A bounce is a discrete value and an even number of bounces are required for the beam to transit through the sample and be collected by the prism at the other end, so n may be rounded down to the nearest even integer. The total path length may be related to the number of bounces by recognizing that the number of times that the beam transits from the bottom of the sample to the top or from the top to the bottom is roughly equal to n. Thus, the total path length, x, may be expressed as follows.

$$x = d/\sin\phi \quad (16)$$

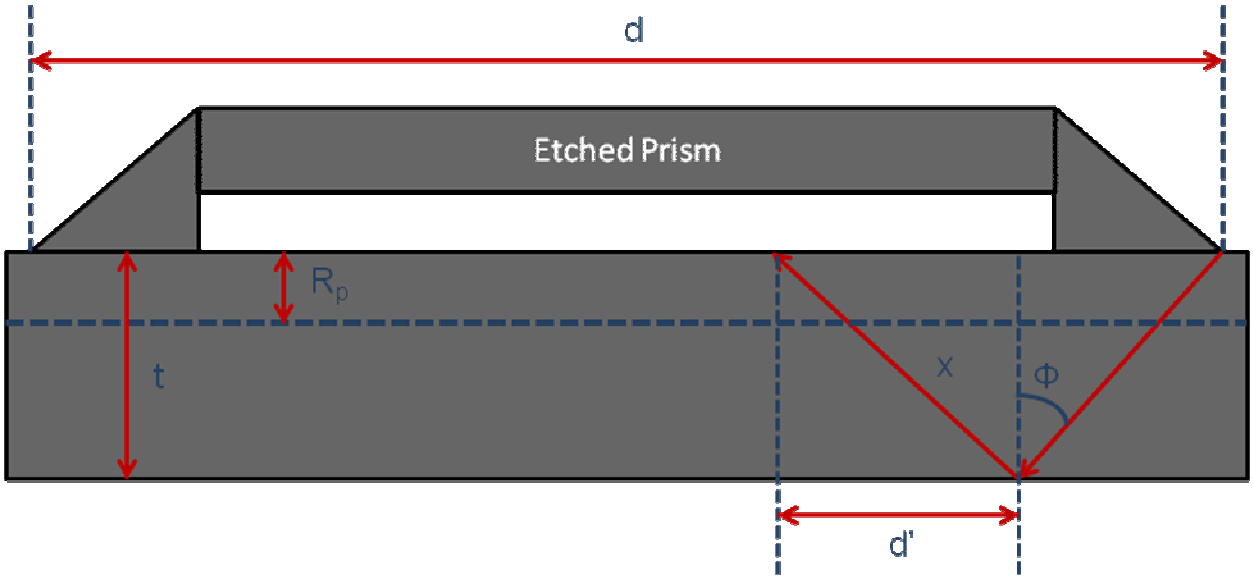

Figure 9: The derivation of the pathlength of the infrared beam through the sample being evaluated using MIT-IR Spectroscopy. The pathlength is equal to the pathlength associated with a single bounce, x, multiplied by the number of bounces, n. the pathlength per bounce is defined by the horizontal travel per bounce, determined by Φ, as well as the sample thickness.

The attenuation of the infrared intensity due to the path taken by the infrared beam through the sample may be expressed by considering several different factors. The ratio of intensity between the incident infrared beam and the beam transmitted through the prism is a fundamental limit to the observed intensity. At each bounce, only a given amount of infrared energy will be reflected back into the sample. A reasonable first order assumption is that all energy not retained by total internal reflection within the sample is lost. For a given material-prism system, depending upon the polarization of the infrared beam as well as the surface roughness of the interfaces, this ratio of the reflected intensity to the transmitted intensity will

vary. By using samples polished on both sides, the effects of surface roughness can be negated, leaving only a dependence upon the polarization of the infrared beam. The resulting variation in reflected intensity for the interface between the prism or sample and the ambient is defined as follows, where Rs is the reflected intensity ratio for a perpendicularly polarized beam and Rp is the reflected intensity ratio for a parallel polarized beam. As before, it is assumed that the extinction coefficient is much smaller in magnitude than the refractive index and, as such, doesn't have an effect on the observed reflectivity. The term □' represents the angle of the transmitted beam which may be expressed using Snell's Law [8] while n_V is the refractive index of the ambient and n_P is the refractive index of the prism.

$$Rs = \left(\frac{n_P \sin\phi - n_V \sin\phi'}{n_P \sin\phi + n_V \sin\phi'}\right)^2 \quad (17)$$

$$R_p = \left(\frac{n_V \sin\phi - n_P \sin\phi'}{n_V \sin\phi + n_P \sin\phi'}\right)^2 \quad (18)$$

The Transmission into and out of the prism may be expressed using these same reflectivity terms as the transmission is simply equal to 1-R. In the case of transmission into the prism, the incident angle of the infrared beam replaces the reflected angle off the bottom and top surfaces of the prism and n_V and n_P are switched because the transmitted beam no longer travels from the prism into the ambient, but from the ambient into the prism. In the case of transmission from the prism to the detector, n_V and n_P remain as in the equation and the angle of interest is equal to the difference between the bevel angle, α, and the reflected angle, □. This is equivalent to the angle (□') resulting from the refraction of the incident beam as it passes from the ambient

to the prism. This expression may be derived using Snell's Law for the angle of the incident beam with respect to the prism bevel, □.

The attenuation of the infrared beam due to the bulk of the sample may be determined by applying the Lambert-Beer Law for intensity loss in an absorbing medium. In this derivation, two separate absorption events occur. The sample itself, irrespective of any existing Ion Implant Damage will absorb radiation as this radiation passes through it. The rate at which this absorption occurs over a unit path length is equal to the term γ, which is related to the absorption factor of the refractive index, k, as follows, where λ is the wavelength of the light generated in the ambient. In addition, radiation will be absorbed by any damage resulting from Ion Implantation. The rate at which radiation is absorbed by Ion Implantation Damage per unit pathlength may be expressed as equal to the damage concentration, N_T, multiplied by a capture cross section, σ. In addition, a scaling constant must be multiplied in to account for the ratio of the pathlength over which Ion Implant Damage contributes to absorption as compared to the total pathlength. This term may be expressed as the ratio between the Projected Range of the implant, Rp, and the total sample thickness, t. The sum of these two terms represents an expression for the total attenuation of radiation for a given unit pathlength [9].

$$dI = -I\left[\gamma + \frac{Rp}{t} N_T \sigma\right] dx \quad (19)$$

$$\gamma = \frac{2\pi k}{\lambda} \quad (20)$$

The quantity of light transmitted over the full pathlength of the infrared beam in the sample may be expressed as follows. In this equation, I_0 represents the beam intensity prior to traveling through the prism while I represents the beam intensity only due to Lambert-Beer attenuation after traveling through the sample.

$$I = I_0 \exp\left(-\left[\gamma + \frac{Ep}{t} N_T \sigma\right] x\right) \quad (21)$$

The total attenuation for a non-absorbing sample may be expressed by multiplying the loss due to transmission into and out of the prism by the attenuation due to the absorption of the sample as well as by the total number of reflections off the top and bottom sample surfaces. In the case of a sample with Ion Implant Damage, the Beer-Lambert Law requires that both the term representing the absorption of the bulk sample, γ, and the term representing the absorption due to Ion Implant Damage be included. This is not the case for a baseline sample, where no Ion Implantation occurs and only γ must be included. The resulting terms for the attenuation of the beam intensity are as follows, where I_{BL} is the intensity associated with a baseline sample while I_S is the intensity generated by the ion implanted sample.

$$I_{BL} = I_0 \exp\left(-\gamma x\right)\left(1 - R(n_V, n_p, \theta)\right)\left(1 - R(n_p, n_V, \theta')\right)R(n_p, n_V, \phi)^n \quad (22)$$

$$I_S = I_0 \exp\left(-\left[\gamma + \frac{Ep}{t} N_T \sigma\right] x\right)\left(1 - R(n_V, n_p, \theta)\right)\left(1 - R(n_p, n_V, \theta')\right)R(n_p, n_V, \phi)^n \quad (23)$$

It is worth noting that division of the spectrum of a sample with the states of interest by a baseline standard without any states will result in a differential spectrum which may be used for analysis. Rp, t, x (defined in Equation 10) and, ideally, σ, may be considered constant. Thus, after taking the natural logarithm of the ratio between the infrared signal generated by absorption in the implanted sample and the baseline infrared signal, an expression may be derived that directly correlates the density of particular species of ion damage to the intensity ratio of an ion implanted sample to a baseline sample. This expression is as follows.

$$N_T = -\frac{t}{\sigma x Rp} \ln\left(\frac{I_S}{I_{BL}}\right) \quad (24)$$

1.5: Hydrogen Implant Defects in Semiconductors

A variety of studies have been performed in order to observe the structural and electronic defects arising from Hydrogen Implantation or Hydrogen-Helium Co-Implantation, both for low-fluence studies as well as for ion cutting related studies.

Structural defect studies have included such analytical techniques as Transmission Electron Microscopy (TEM), Atomic Force Microscopy (AFM), Rutherford Backscattering Spectroscopy (RBS), and Multiple Internal Transmission Infrared (MIT-IR) Spectroscopy. The effects of Hydrogen Implantation and Hydrogen-Helium Co-Implantation as studied by MIT-IR were of particular interest in relation to this study MIT-IR has picked up vibrational modes and bending modes of a variety of states. These states include trapped molecular hydrogen and hydrogen-bonded interfaces corresponding to crystal facets of dislocation loops. These states

correspond to 2084 wavenumbers for the <111> facet and 2110 for the <100> facet. In addition, ATR-IR Spectroscopy has detected the presence of monovacancies decorated with anywhere from one to four hydrogen atoms as well as decorated multivacancies, particularly hydrogen-decorated divacancies possessing anywhere from one to six bonded hydrogen atoms. VH, VH2, VH3, and VH4 have been observed to possess stretching modes in the 2025, 2125, 2161/2188 and the 2219 wavenumber ranges, respectively. The presence of hydrogen-decorated silicon interstitial defects has also been postulated based on the presence of resonant states in the 2000 to 1950 wavenumber range [10].

Electronic defect studies have included studies at room temperature of pseudo-doping effects using techniques such as Hall Effect Resistivity and Hall Effect Mobility as well as Four Point or Two Point Probe Resistivity. These studies have observed several general trends in carrier density with respect to annealing temperature. Hall Effect Resistivity studies have demonstrated that p-type samples implanted with Hydrogen or a Hydrogen-Helium combination at high fluences maintain their p-type behavior up until approximately 450°C, at which point a predominance of n-type traps, called thermal donors, compensate and invert the semiconductor material. This effect is maintained until approximately 500°C, at which point the majority of thermal donors begin to dissociate, leaving in their wake the background p-type doping of the semiconductor as well as a host of thermal acceptors which remain stable at elevated annealing temperatures up to around 700°C. The result of this effect is the presence of hole carrier concentrations in excess of the background doping.

Cryogenic Studies have made use of Electron Paramagnetic Resonance as well as Laplace DLTS and traditional DLTS methods to detect specific energy levels and capture cross-sections associated with deep level traps [3]. Analysis of Hydrogen Implantation defects has

largely been confined to study of electron trapping in n-type materials. Hydrogen implanted n-type materials manifest themselves in a variety of configurations. VH_1, a single vacancy decorated with a single hydrogen atom manifests itself as an electron trap with an activation energy for emission corresponding to .43eV to .44eV. An electron trap with an emission activation energy of .49eV has been validated experimentally and theoretically as a V_2H decorated divacancy defect. The VO defect, corresponding to a vacancy-oxygen bond is transformed from a .15eV electron trap center to a .32eV electron trap after thermal annealing. VH, and V2H have been observed to decay after thermal annealing in the range of 500°C to 550°C while VOH requires more thermal energy for the dissociation reaction to take place, not annealing out until around 600C°. VH possesses very similar symmetry to a similar defect, VP, which is the defect arising from incomplete activation of a phosphorus atom in a vacancy site. This has led to some speculation that VH acts as a "Pseudo Group V Element" [11].

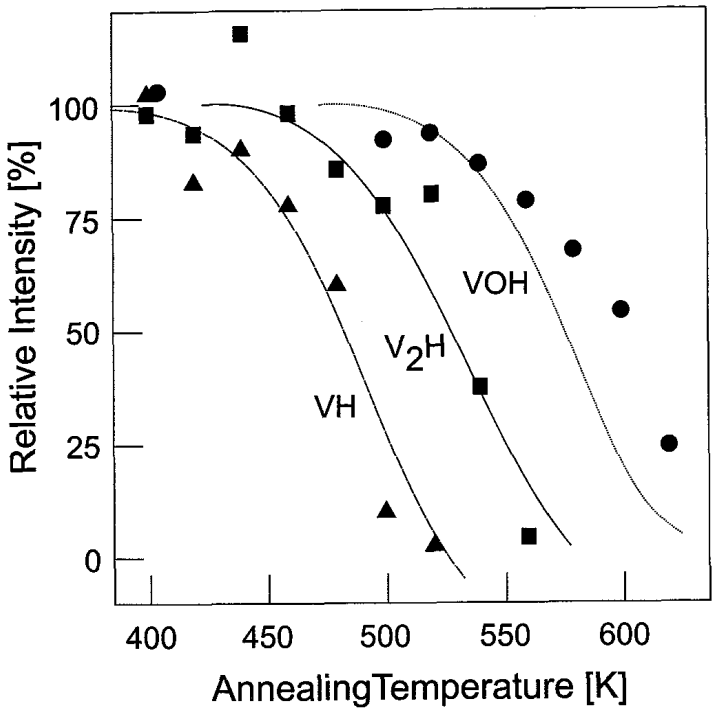

Figure 10: Annealing behavior of electron traps generated by H^+ implantation [11].

Some investigation of hydrogen-induced acceptor states has occurred. However, the acceptor states arising from hydrogen implantation have not been studied in nearly as much detail. There is little understanding of the structural imperfections that lead to these defects. A defect at .28eV above the valence band has been observed by multiple authors and the possibility of this defect being caused by hydrogen bonding has been discussed. However the similarities in annealing characteristics between this defect and the Ci-Oi (or carbon-oxygen interstitial bond) defect has ruled this possibility out [12]. An additional defect at .51eV above the valence band has also been observed. This defect is currently attributed to a boron-hydrogen interstitial complex [13]. Two additional traps existing at .33eV and .66eV have been extracted using

DLTS and the proposal has been made that these defects correspond to VH_2 and VH_3 defects, respectively [14].

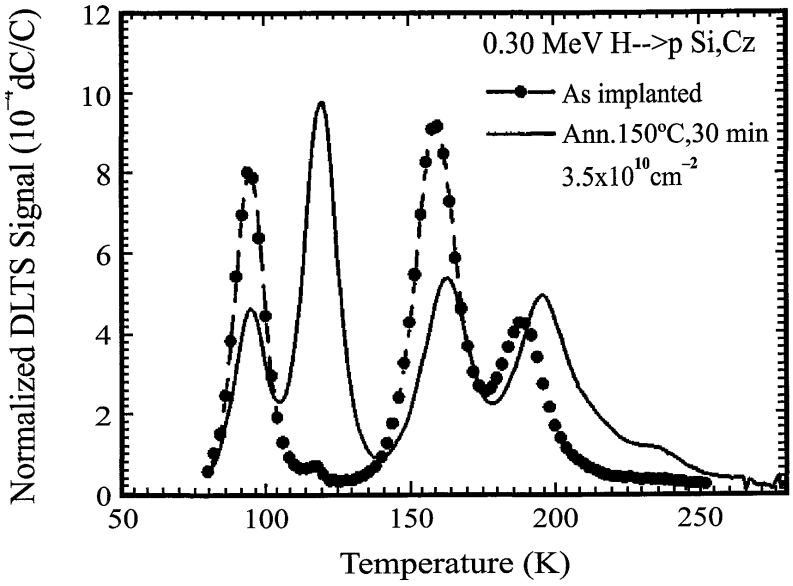

Figure 11: DLTS Spectra of an as-formed P-Type sample implanted with H+ ions at 300 KeV [13].

The presence of interstitial Carbon-Oxygen as well as unbounded Vacancy defects may also be expected to contribute to signals arising from Hydrogen or Hydrogen-Helium Implantation experiments by virtue of the fact that any physical bombardment of a Cz-grown sample will induce point defects including vacancies, silicon interstitials, interstitial dopant atoms and interstitial carbon and oxygen. Vacancy defects do not have a single charge state. Rather, they may exist in a positive state, which decays to neutrality (V^+ corresponding to .05eV+E_V) or negative charge state, which decays to neutrality (V^- corresponding to .32eV-E_C) as well as a double positive charge state which decays to a positive state (V^{++} corresponding to

.13eV+E_V) [3]. As stated earlier, interstitial carbon has been found to exist in a state corresponding to .28eV above the valence band as well as in a state corresponding to .1eV below the conduction band [12]. Interstitial carbon may also bond with substitutional carbon to form a C_i-C_s bond with an energy corresponding to .33eV above the valence band [15]. An additional state, corresponding to a substitutional carbon bond with a divacancy exists at .09eV below the conduction band and has demonstrated bistability [16]. After annealing at a temperature of 300°C or more, this state decays, yielding a new state at .17eV below the conduction band [17]. Carbon may bond with Oxygen in an interstitial configuration to form a C_i-O_i bond corresponding to a state at .38eV above the valence band [18].

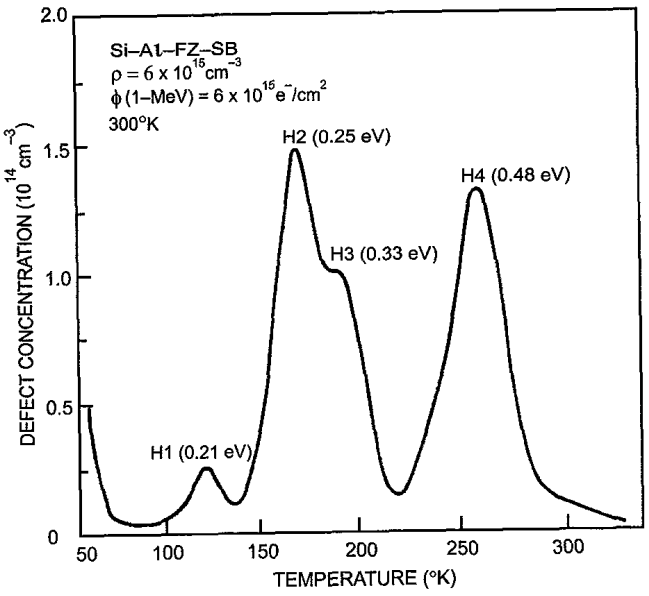

Figure 11: DLTS Spectra of hole traps in P-Type Silicon silicon implanted with Silicon at 1MeV [3].

Chapter 2: DLTS Fitting Functions

2.1: Simplifications to the Charge Transient

The dual-boxcar technique used in DLTS to produce a signal is a method of discrete differentiation with respect to time. This is accomplished by subtracting the signal being measured at two separate times. With this in mind, it stands to reason that a fitting function for the resulting discrete differential could be produced simply by differentiating the trap capture/emission function listed above with respect to the emission time and that this fitting function may be accurate as a first order approximation. The result of such a differentiation is as follows, bearing in mind that the kinetic rates described below only apply to conditions inherent to the emission pulse, not the filling pulse.

$$\frac{dp_T}{dt} = -p_{T0}(K_n + K_p)e^{[-(K_n+K_p)t_D t(1,2)]} \quad (1\text{-}1)$$

$$\frac{dn_T}{dt} = -n_{T0}(K_n + K_p)e^{[-(K_n+K_p)t_D t(1,2)]} \quad (1\text{-}2)$$

These equations are adequate to describe the resulting transient of an I-DLTS measurement since the current is literally the differential of the trapped charge concentration with respect to time.

In the case of a capacitive or voltage-based measurement, this differentiation must be converted to a change in trapped carrier concentration alone, which is accomplished by separating the change in time from the change in trapped carrier concentration as follows where

the change in time, Δt, is equal to the difference between $t_D t_1$ and $t_D t_2$. In this case, the function, t, is the average of $t_D t_1$ and $t_D t_2$.

$$\Delta p_T = -p_{T0}\Delta t(K_n + K_p)e^{-(K_n+K_p)t} \quad (2\text{-}1)$$

$$\Delta n_T = -n_{T0}\Delta t(K_n + K_p)e^{-(K_n+K_p)t} \quad (2\text{-}2)$$

The result of this differentiation is a peaked function. It is readily observable that the function described here has a magnitude which is dependant not only on the conditions and duration of the filling pulse (indicated by p_{T0} and n_{T0}), but also by the rate of capture and emission of carriers during the emission pulse.

This function is a reasonable first-order approximation of the true DLTS signal resulting from a voltage-based or capacitive measurement, which is a discrete differential. This equation is as follows.

$$\Delta p_T = p_{T0}\left(e^{[-(K_n+K_p)t_D t_2]} - e^{[-(K_n+K_p)t_D t_1]}\right) \quad (3\text{-}1)$$

$$\Delta n_T = n_{T0}\left(e^{[-(K_n+K_p)t_D t_2]} - e^{[-(K_n+K_p)t_D t_1]}\right) \quad (3\text{-}2)$$

In this discrete form, t_1 and t_2 represent the first and second times at which the emission transient is sampled through boxcar integration.

These equations remain complex, even when simplified to the first order approximation given by the differential form listed above. If further reduction of the equation is required, it is reasonable in some circumstances to assume that the rates described above may be simplified by reducing the four-rate equations above down to two or possibly one rate.

The law of mass action necessitates that in any semiconductor where the Fermi Energy is significantly displaced from the intrinsic energy only one carrier type will be present in large numbers within the material. Thus, in the case of a trap existing at a point where the Fermi Energy is significantly displaced from the intrinsic energy, only one capture rate will dominate and the other may be neglected. The criteria for this transition from a two-rate capture kinetic to a single-rate kinetic is a point where the capture rate for one carrier is less than one tenth of the capture rate for the other carrier. By invoking the law of mass action and separating the capture kinetics into their constituent capture cross-sections and thermal velocities, the following equations may be defined for the hole concentration (electron concentration) required for the dominance of the electron capture kinetic (hole capture kinetic).

$$p < n_i \left[\frac{\sigma_n v_n}{10 \sigma_p v_p} \right]^{1/2} \quad (4\text{-}1)$$

$$n < n_i \left[\frac{\sigma_p v_p}{10 \sigma_n v_n} \right]^{1/2} \quad (4\text{-}2)$$

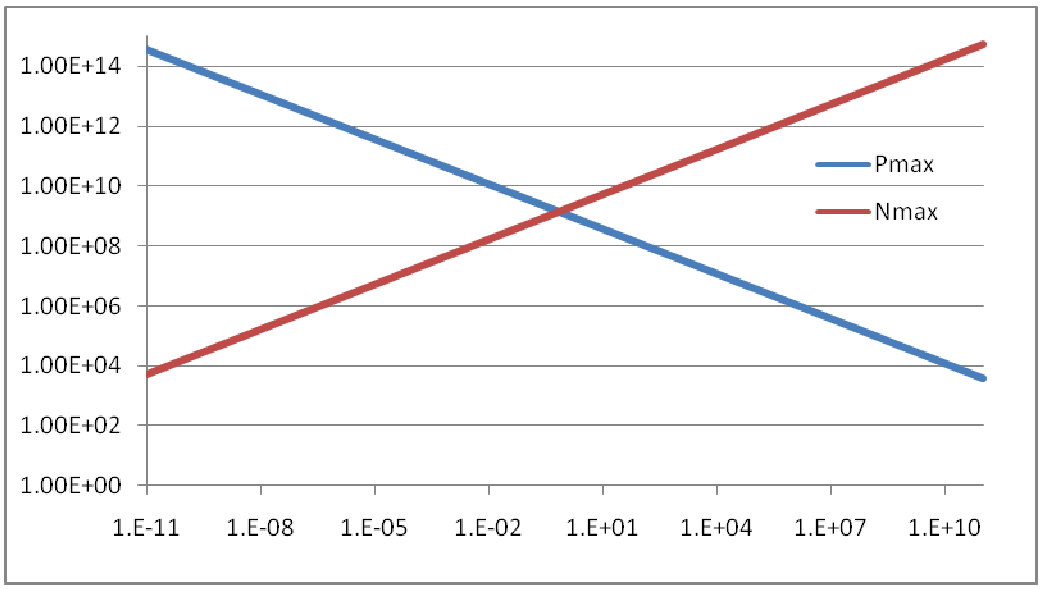

Figure 1: The maximum minority carrier concentrations permissible in a semiconductor in order for one capture rate to dominate in a DLTS measurement (4-1 and 4-2). This dependence is related to the ratio between the hole capture cross section and the electron capture cross section and corresponds to the maximum carrier concentrations permissible for carriers to fill trap states during an emission pulse.

It is possible for both capture terms to remain dominant in comparison to one another in cases where the Fermi Energy approaches the intrinsic energy. However, in such a situation, the emission rates associated with thermal emission of carriers from the trap will dominate the rates associated with carrier capture, and both capture rates may be ignored.

The criteria for a case where the capture rates for a given trap are sufficiently small in comparison to their corresponding emission rates is where the capture rate is less than one tenth of its corresponding emission rate. This may be expressed in terms of carrier concentrations or in terms of the energy level of the trap in question. Expressing this criteria in terms of the electron or hole concentration yields the following equations, where the term γ is the product of the thermal velocity, the density of states and the squared inverse temperature.

$$p < \frac{1}{10}\frac{\gamma_p}{v_p}T^2 e^{-(E_T - E_V)/kT} \quad (5\text{-}1)$$

$$n < \frac{1}{10}\frac{\gamma_n}{v_n}T^2 e^{-(E_C - E_T)/kT} \quad (5\text{-}2)$$

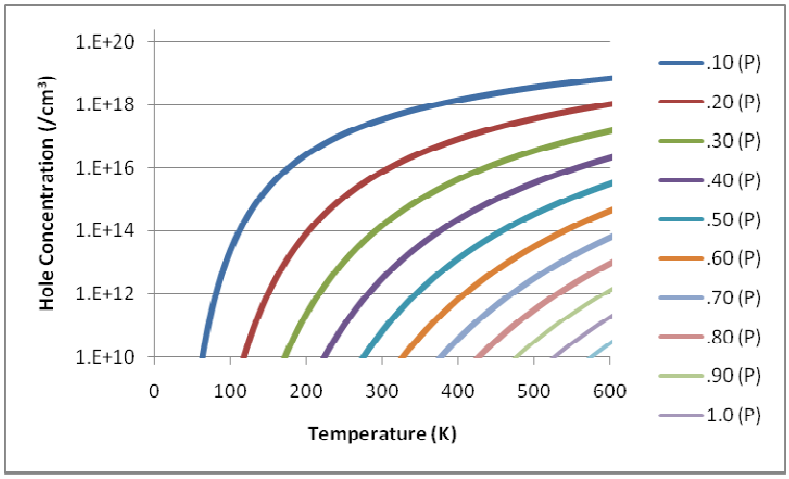

Figure 2: The maximum hole concentration for trap emission to occur with varying temperature and varying trap energy barriers (5-1 and 5-2). Given the behavior of Boltzmann Statistics, the observed trends (namely that the maximum hole concentration increases with temperature and decreases with energy barrier) are to be expected.

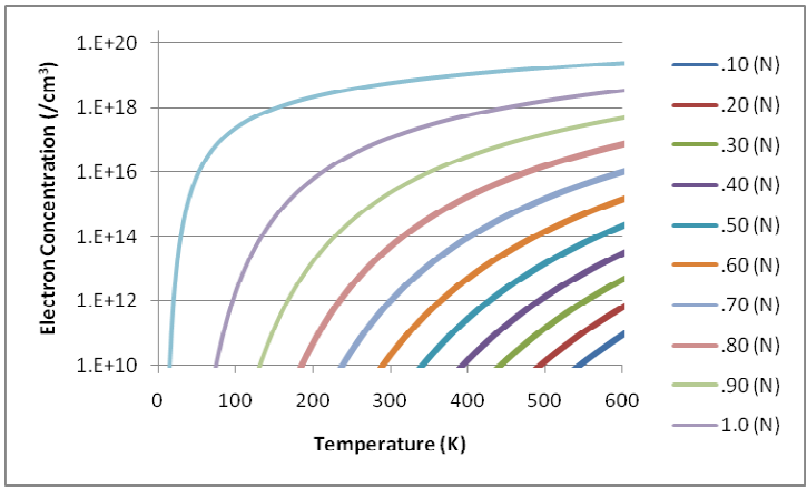

Figure 3: The maximum electron concentration for trap emission to occur with varying temperature and varying trap energy barrier (5-1 and 5-2). Given the behavior of Boltzmann Statistics, the observed trends (namely that the maximum electron concentration increases with temperature and decreases with energy barrier) are to be expected.

It is important to note that the dominance of any emission term over its corresponding capture term is completely independent of the capture cross-section of the trap species in question. The preceding criteria may be re-expressed for the trap energy as follows.

$$E_T < kT\left[\ln(10\gamma_p T^2) - \ln(v_p p)\right] + E_V \quad (6\text{-}1)$$

$$E_T > E_C - kT\left[\ln(10\gamma_n T^2) - \ln(v_n n)\right] \quad (6\text{-}2)$$

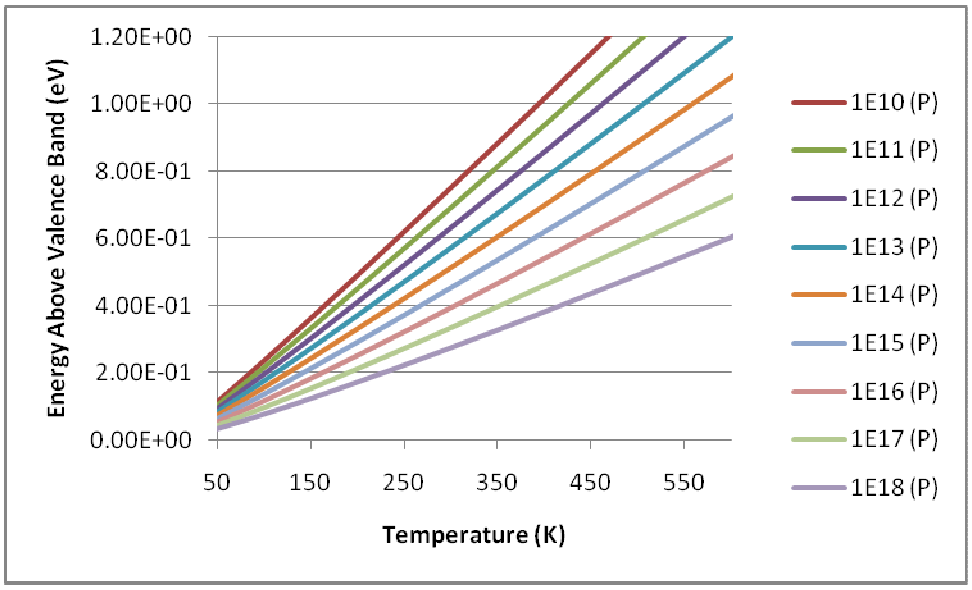

Figure 4: Variation of the maximum energy level resolvable with respect to the valence band for thermal acceptor emission with respect to temperature and hole concentration within semiconductor (6-1 and 6-2). As temperature increases, the maximum resolvable energy level also increases, as expected. It is also expected that the maximum resolvable energy level decreases with respect to hole concentration.

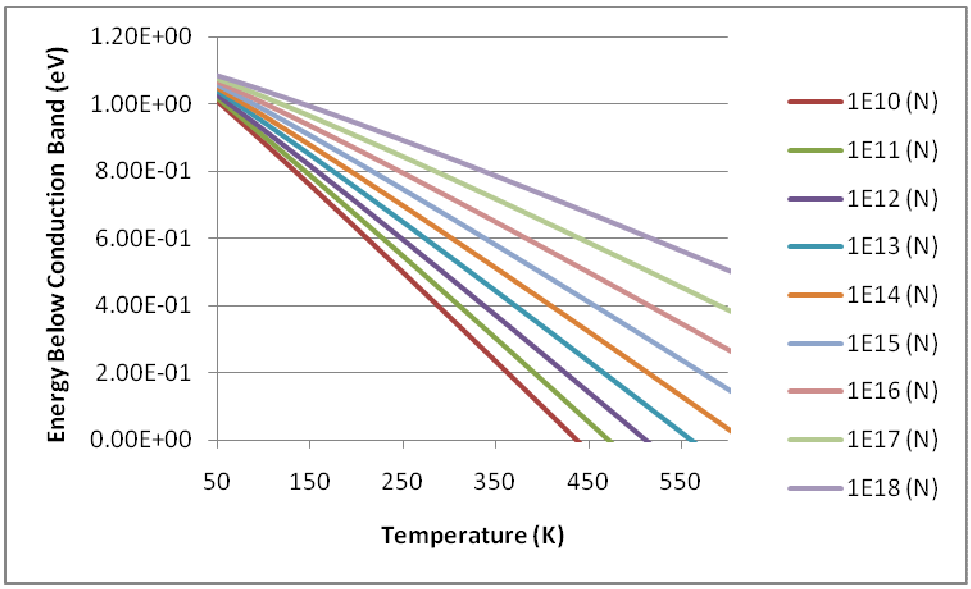

Figure 5: Variation of the minimum energy level resolvable with respect to the conduction band for thermal donor emission with respect to temperature and electron concentration within semiconductor (6-1 and 6-2). As temperature increases, the minimum resolvable energy level also decreases, as expected. It is also expected that the maximum resolvable energy level increases with respect to electron concentration.

It is typically the case that one emission term will dominate over the other term for any trap with an energy level sufficiently larger or smaller than the energy associated with mid-gap. For states existing near the mid-gap energy or for states with sufficiently large differences in hole and electron capture cross-sections, it may not be readily apparent as to whether one emission term dominates over the other or if both emission terms remain dominant. It may be assumed that only one emission rate will remain dominant if one of the two emission rates is less than one tenth the magnitude of the other rate. With this criterion in mind, the trap energy required for one emission rate to dominate is as follows.

$$E_T < \frac{1}{2}\left[E_c + E_V - \ln\frac{\gamma_n \sigma_n}{10\gamma_p \sigma_p} \right] \quad (7\text{-}1)$$

$$E_T < \frac{1}{2}\left[E_c + E_V - \ln \frac{\gamma_p \sigma_p}{10 \gamma_n \sigma_n} \right] \quad (7\text{-}2)$$

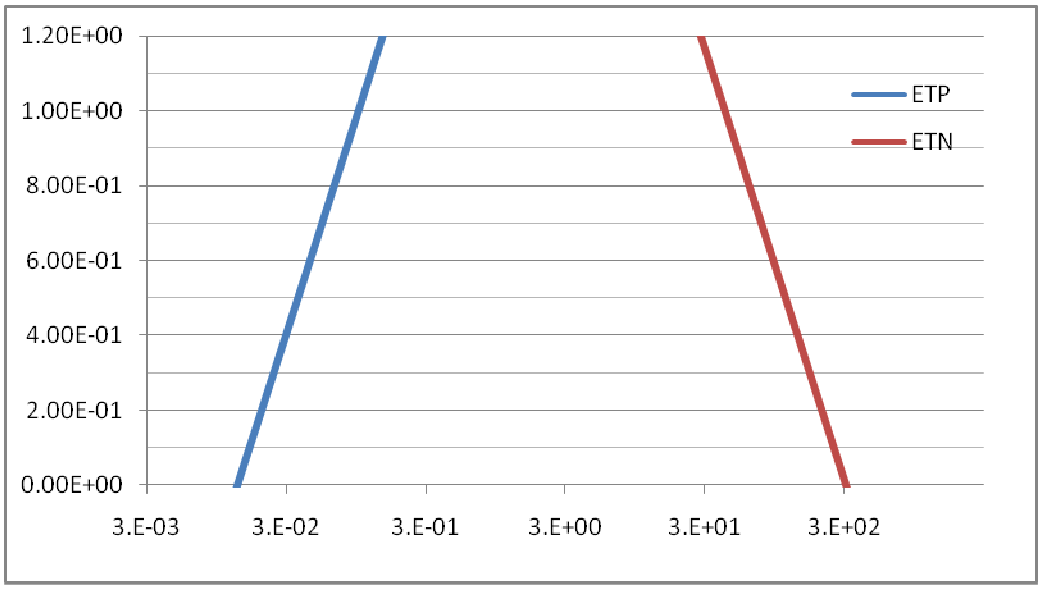

Figure 6: The maximum resolvable energy gap for a hole or electron trap with respect to the capture cross section difference associated with the hole and electron emission rates (7-1 and 7-2). It is to be expected that as the ratio between hole and electron capture cross section increases, the maximum resolvable energy gap for holes increases while the maximum resolvable energy gap for electrons decreases.

In the case of a metallurgical junction where ionized charge exists largely on one side or the other, two separate regions may be presumed to exist. Where the depletion approximation is accurate, a region where emission dominates over capture exists. In this region, the minority carrier capture rate may also dominate, especially near the metallurgical junction. However, because the minority carrier capture cross-section is typically quite small, the minority carrier capture rate is typically dominated by the majority carrier emission rate. As a consequence, only one rate is dominant in this region. For trap levels with energies away from mid-gap where the depletion approximation is valid, the following equations are applicable.

$$\Delta p_T = -\Delta t p_{T0} e_p e^{-e_p t} \quad (8\text{-}1)$$

$$\Delta n_T = -\Delta t n_{T0} e_n e^{-e_n t} \quad (8\text{-}2)$$

Similarly, the following equations result for the discrete form of the DLTS signal.

$$\Delta p_T = p_{T0}\left(e^{-e_p t_D t_1} - e^{-e_p t_D t_2}\right) \quad (9\text{-}1)$$

$$\Delta n_T = n_{T0}\left(e^{-e_n t_D t_1} - e^{-e_n t_D t_2}\right) \quad (9\text{-}2)$$

As the depletion approximation begins to fail near the edge of the depletion region, a second region exists where capture may no-longer be neglected. In the case where the depletion approximation is not valid, the majority carrier capture rate may not be ignored and the following equations apply. It is important to note that while this is, technically the form observed for regions near the depletion edge, the filling dynamic of the trap levels within this region leads to incomplete or no filling.

$$\Delta p_T = -\Delta t p_{T0} (e_p + c_p) e^{-(e_p + c_p)t} \quad (10\text{-}1)$$

$$\Delta n_T = -\Delta t n_{T0} (e_n + c_n) e^{-(e_n + c_n)t} \quad (10\text{-}2)$$

The following equations result for the discrete form of the DLTS signal.

$$\Delta p_T = p_{T0}\left(e^{-(e_p + c_p)t_1} - e^{-(e_p + c_p)t_2}\right) \quad (11\text{-}1)$$

$$\Delta n_T = n_{T0}\left(e^{-(e_n+c_n)t_1} - e^{-(e_n+c_n)t_2}\right) \quad (11\text{-}2)$$

It is important to note that in the case of a trap which exists close to mid-gap, no assumptions can be made regarding the dominance of emission or capture rates for either carrier, and the full form of the equation must be used.

The terms p_{T0} and n_{T0} remain complex due in large part to the transient phenomena involved in the filling pulse. Several simplifications may be made to these terms in order to reduce the overhead inherent in calculation. The terms described may be simplified substantially if flat-band conditions are assumed during the filling pulse.

The filling pulse is typically not performed such that flat-band conditions are achieved throughout the semiconductor. Often, some depletion effects remain at the metallurgical junction. As a result, areas exist where traps are not filled during the filling pulse and, as a result, no emission occurs. There are also regions where filling is not complete as a consequence of partial depletion and, as a result, attenuation of the DLTS signal occurs. These two cases are structural considerations and may be partially approximated with an attenuation factor, as will be discussed in a later section.

In the case of filling of majority carriers and emission of minority carriers, it may be assumed that all majority carrier traps will be filled and all minority carrier traps will be emptied during the capture pulse conditions given an infinite time for filling. A related assumption is that all minority carrier traps will be filled and all majority carrier traps will be emptied during the emission pulse if the pulse is allowed to run to completion. The assumptions are reversed for the filling of minority carriers and emission of majority carriers.

The resulting expressions may be derived for the constants expressed in the above differential forms, again assuming that holes are the majority carriers and electrons are the minority carriers. It is also assumed that majority carriers are being filled during the filling pulse as opposed to the minority carriers.

$$p_{TO} = 1 - e^{-(K_n^f + K_p^f)t_f} \quad (12\text{-}1)$$

$$n_{TO} = 1 - e^{-(K_n^f + K_p^f)t_f} \quad (12\text{-}2)$$

As in the treatment above, the kinetic terms contained within the exponential may be simplified to aid calculation if a few assumptions are made. In the case of capture, the key assumption is that enough charge is injected such that one capture rate dominates the signal. In such a case, the capture rate alone may be input into the terms above and the following terms result, again assuming that holes represent the majority carrier and electrons represent the minority carrier. As above, the terms may be reversed if minority carriers are being filled during the filling pulse.

$$p_{TO} = 1 - e^{-c_p t_f} \quad (13\text{-}1)$$

$$n_{TO} = 1 - e^{-c_n t_f} \quad (13\text{-}2)$$

In the case of shallow level traps or of higher temperatures approaching 300K, the emission term cannot be neglected and the assumption that the steady-state boundary condition of the

transient is that of a completely filled concentration should be called into question. The resulting filling term may be expressed as follows.

$$p_{TO} = 1 - e^{-(e_p + c_p)t_f} \quad (14\text{-}1)$$

$$n_{TO} = 1 - e^{-(e_n + c_n)t_f} \quad (14\text{-}2)$$

The resulting equation for the differential charge observed during DLTS uses these final forms of the filling function combined with the differentials where the depletion approximation applies.

$$\Delta p_T = -\Delta t(1 - e^{-(e_p + c_p)t_f})e_p e^{-e_p t} \quad (15\text{-}1)$$

$$\Delta n_T = -\Delta t(1 - e^{-(e_n + c_n)t_f})e_n e^{-e_n t} \quad (15\text{-}2)$$

The discrete form of this differential is as follows.

$$\Delta p_T = (1 - e^{-(e_p + c_p)t_f})(e^{-e_p t_D t_2} - e^{-e_p t_D t_2}) \quad (16\text{-}1)$$

$$\Delta n_T = (1 - e^{-(e_n + c_n)t_f})(e^{-e_n t_D t_1} - e^{-e_n t_D t_2}) \quad (16\text{-}2)$$

Chapter 3: DLTS Analysis of MIS Capacitor Structures

3.1: The Structure of MIS Capacitors

Two subsets of trap states are commonly observed in MIS Capacitors. The first of these are interface states, which are spatially localized at the interface between the semiconducting crystal and the insulator, but energetically variable because of the variety of bonding configurations available to a defect at an interface between an amorphous material and a crystalline material. Bulk trap states are also commonly seen in MIS structures. These states contain discrete energy levels determined by trap species but vary spatially throughout the semiconductor crystal. In order to derive the activity of these trap states, the activity of the Fermi Energy and the activity of associated free carriers with applied bias must be considered [19].

In MIS capacitors, the magnitude of the Fermi Level with respect to position in the semiconductor is derived from the solution to the Poisson Equation. It is assumed that the structure exists on a semiconductor with spatially constant doping and with a trap concentration which is assumed to be at most one tenth that of the doping or less. This level of ionized charge is considered small enough that it will not substantially modify the Poisson Equation and, in doing so, not affect the time-dependant behavior of the Fermi Energy in relation to the bent bands within the semiconductor.

The potential distribution solution to the Poisson Equation is approximately parabolic for the case stated above. The bending of the bands of the semiconductor in relation to the Fermi-Level may be defined as follows when the MIS Capacitor is biased into depletion [20].

$$\phi(x) = \frac{\phi_S}{W^2}(W - x)^2 \quad (1)$$

Where x is the depth into the semiconductor, ϕ_s is the surface potential and W is the width of the depletion region, a region where free majority carriers have been swept out of the semiconductor by an internal electric field, leaving only minority carriers as well as ionized donors and acceptors. The expression for the depletion width is as follows [20].

$$W = \left[N_A - N_T(t)\right]^{-1/2}\left(\frac{q}{2\varepsilon_s\phi_s}\right)^{-1/2} \quad (2)$$

N_A is the net concentration of donors and acceptors in the semiconductor. N_T is the summed concentration of bulk traps in the semiconductor, $Q_{B,}$ divided by the width of the depletion region, which is assumed to remain relatively constant despite the change in ionized charge concentration over time. The term q is the fundamental charge of an electron and ε_s is the permittivity of the semiconductor. Analysis of this depletion width is greatly simplified with little loss of accuracy if it is assumed that the steady state trapped charge concentration has little effect on the width of the depletion layer and that the transient trapped charge concentration has a negligible effect on band bending.

The free carrier concentration varies exponentially with the band bending in relation to the Fermi Level. This is due to the fact that the band bending linearly affects the offset of the Fermi Energy in relation to the conduction and valence bands of the semiconductor[2]. This free

carrier concentration may be related either to the intrinsic energy level and carrier concentration or to the Dopant Concentration and associated Fermi Energy.

$$p = n_i e^{[E_i - E_F - q\phi_S]/kT} \quad (3\text{-}1)$$

$$n = n_i e^{[E_F - E_i + q\phi_S]/kT} \quad (3\text{-}2)$$

With the preceding information about the free carrier concentration, a function may be derived to express the transient activity of both interface states and bulk states. Bearing in mind that the interface states are fixed spatially but variable energetically, the following integrals may be defined and solved for numerically [21].

$$\Delta Q_{is}^{n} = \left[\int_{E_V}^{E_C} N_T(E) * \Delta n_T(\phi^f, \phi^e, E) dE \right]_{x=0} \quad (4\text{-}1)$$

$$\Delta Q_{is}^{p} = \left[\int_{E_V}^{E_C} N_T(E) * \Delta p_T(\phi^f, \phi^e, E) dE \right]_{x=0} \quad (4\text{-}2)$$

Q_{is} is defined as the density (per square centimeter) of interface states, which is shown to vary with respect to the potential at the surface (x=0) during the filling and emission pulses as well as with the energy (E).

Over time during the filling and emission pulses, Q_{is} will change as trap states emit or capture. In the case of electron-filled traps, all states existing below the Fermi Level will remain

thermodynamically stable, but all states existing above the Fermi Energy will become thermodynamically unstable and begin to emit carriers. All hole traps existing above the Fermi Level will remain thermodynamically stable and all states below this level become thermodynamically unstable and emit over time. Because of this effect, the positions of the Fermi Energy at the interface during the filling and emission pulses defines the energy range over which interface states will be filled and emitted. The resulting integral of this variable distribution is as follows, with ϕ_f representing the position of the Fermi Energy during the filling pulse and ϕ_e representing the position of the Fermi Energy during the emission pulse [21].

$$\Delta Q_{is}^{n} = \left[\int_{q\phi_v}^{q\phi_f} N_T(E) * \Delta n_T(\phi_s^f, \phi_s^e, E) dE \right]_{x=0} \quad (5\text{-}1)$$

$$\Delta Q_{is}^{p} = \left[\int_{q\phi_f}^{q\phi_e} N_T(E) * \Delta p_T(\phi_s^f, \phi_s^e, E) dE \right]_{x=0} \quad (5\text{-}2)$$

Bearing in mind that bulk states are fixed energetically but variable spatially, the following integrals may be defined for a single trap species at E_T within the bulk, Q_B.

$$\Delta Q_{B}^{p} = \left[\int_{0}^{\infty} N_T(x) * \Delta p_T(\phi_s^f, \phi_s^e, x) dx \right]_{E=E_T} \quad (6\text{-}1)$$

$$\Delta Q_{B}^{n} = \left[\int_{0}^{\infty} N_T(x) * \Delta n_T(\phi_s^f, \phi_s^e, x) dx \right]_{E=E_T} \quad (6\text{-}2)$$

It is trivial to recognize that because band bending cannot occur beyond the maximum depletion width for the MIS Capacitor, the bounds of the integral may be truncated, yielding the following result where W_i is the depletion width at the onset of strong inversion.

$$\Delta Q_B^p = \left[\int_0^{W_i} N_T(x) * \Delta p_T(\phi_s^f, \phi_s^e, x) dx \right]_{E=E_T} \quad (7\text{-}1)$$

$$\Delta Q_B^n = \left[\int_0^{W_i} N_T(x) * \Delta n_T(\phi_s^f, \phi_s^e, x) dx \right]_{E=E_T} \quad (7\text{-}2)$$

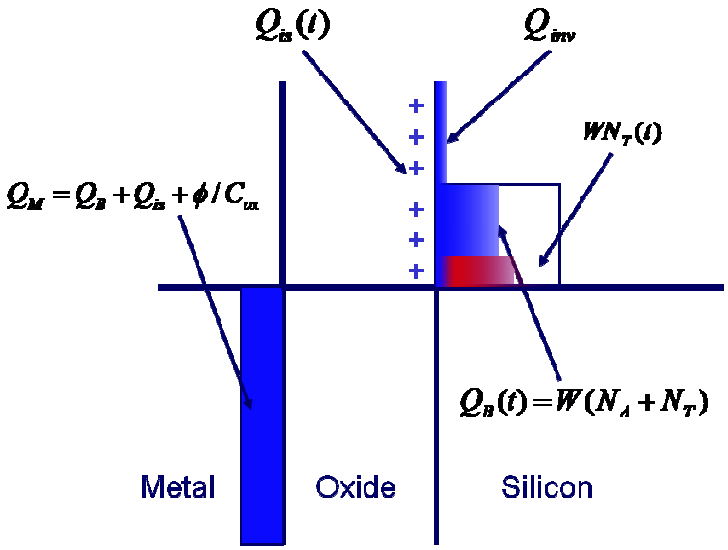

Figure 1: The charge structure of an MIS Capacitor – Contributions to the charges within the MIS structure include the bulk charge, formed by the ionized dopant and impurity atoms contained within the depletion region, the interface trapped charge and the sheet of charge contained within the inversion layer. This charge is mirrored in the gate.

This inversion-defined depletion width is equal to the depletion width where the surface potential equates to twice the Fermi potential defined by the doping of the semiconductor portion of the MIS structure. Thus, the inversion-defined depletion width is equal to the following [20].

$$W_i = \left[N_A - N_T(t)\right]^{-1/2}\left(\frac{q}{4\varepsilon_s\phi_f}\right)^{-1/2} \quad (8)$$

3.2: DLTS Small Signal Analysis

Yet another consequence of Poisson's Equation is the relation of the capture and emission of trap states on observed signals resulting from DLTS measurements. Voltage as well as current measurements combine the signals from the interface and bulk states in a linear fashion, resulting in a superposition of the two emission events. Capacitance-based measurements add the charge signals from the interface and bulk in parallel, resulting in a radically different signal from the voltage and current measurements in certain regimes.

All DLTS measurements are performed using some sort of technique to achieve a differentiation of a signal with respect to time. In the case of current DLTS, the sensing of the current transient at a given time represents an implicit differentiation of charge with respect to time. In constant capacitance (voltage) DLTS and capacitance DLTS, the measurement is linearly dependent upon differentiated charge as well. In this case, the differentiation is approximated with a boxcar integration technique. All DLTS techniques have their basis in the

observance of charge emission over time. Thus, it is important to arrive at the differential of charge with respect to time.

A summation of all charges existing within the MIS Capacitor which are sensed by the gate electrode may be expressed as follows [23].

$$Q_{MIS} = Q_{MS} + Q_{IF} + Q_{IS} + Q_S \quad (9)$$

In this expression, Q_{MS} represents the charge accumulated at the gate electrode due to a workfunction mismatch between the electrode and the semiconductor. Q_{IF} represents fixed charge within the insulator resulting from ionized contaminants and non-stoichiometries within the insulating film. These defects may be considered thermodynamically stable at DLTS temperatures and at varying voltages. Q_{IS} represents the aforementioned charge due to ionized interface trap states while Q_S represents the combined charge of the ionized bulk trap states, Q_B, and the ionized dopants, Q_D, within the depletion layer of the MIS structure. Q_D may be related to the concentration N_A by multiplying by the thickness of the depletion layer, W.

Of the charges listed in the preceding equation for the accumulated charges within an MIS structure, both Q_{MS} and Q_{IF} remain at equilibrium regardless of biasing conditions and may, therefore, be considered invariant with respect to time. The resulting equation contains expressions only for charges due to ionized interface states, ionized bulk states and ionized dopants.

During DLTS measurements at temperatures above approximately 20K, dopant freeze-out has a negligible effect and the ionization of dopants to form the depletion layer is fast enough to

be considered undetectable. The result is the following expression for an I-DLTS measurement in an MIS Capacitor where I_{IS} and I_B are the temporal differentials of interface trap states and bulk trap states, respectively.

$$I_{DLTS} = I_{IS} + I_B \quad (10)$$

The DLTS signal achieved through a boxcar differentiation technique is merely two charge levels taken at two separate times, represented below.

$$\Delta Q_{DLTS} = \Delta Q_{IS} + \Delta Q_B \quad (11)$$

In the case of voltage-based measurements, the signal measured is the additive voltages within the MIS structure due to the charges expressed above. By an application of Gauss' Law, the following expression may be achieved for the observed voltage within an MIS structure [19]. It is important to note that while the charge transients expressed above in (11) are correct, they represent the change in neutral trap levels, which have no charge and cannot be sensed. The observable changes in charge levels in an electrostatic DLTS measurement are those which are ionized by an emission event. Thus, the true density of charge sensed in a Voltage or Capacitive DLTS measurement is equal to the difference between the total concentration of trap states and the filled trap states [23].

$$V_{MIS} = \phi_{MS} + \phi_S + \phi_I \quad (12)$$

In the above expression, Φ_{MS} is an expression of the resultant potential due to workfunction mismatches between the electrode and semiconductor. The term Φ_S represents the surface potential placed upon the semiconductor, which is also the voltage dropped over the entirety of the semiconductor. Lastly, Φ_I represents the voltage taken across the insulating layer. This voltage is the summation of the ionized dopants and bulk traps within the depletion layer divided by the insulator capacitance.

During Constant Capacitance DLTS (CCDLTS), the surface voltage is maintained at a constant value through the use of a capacitance-based feedback loop. The workfunction difference between the semiconductor and electrode is invariant with voltage, so that the only signal observed during CCDLTS is due to the charge sensed through the insulator, Φ_I. The resulting equation is as follows, with Q_D defined as the trapped charge within the insulator [19].

$$V_{CCDLTS} = \frac{Q_D + (WN_A - Q_B) + (N_{IS} - Q_{IS})}{C_{ox}} \quad (13)$$

For the sake of convenience, the total number of filled states existent between the surface potentials defined by the filling pulse and the emission pulse are stated as equal to N_{IS}. The DLTS signal achieved through a boxcar differentiation technique is merely two CCDLTS voltages taken at two separate times, represented below.

$$\Delta V_{CCDLTS} = -\frac{\Delta Q_{IS} + \Delta Q_B}{C_{ox}} \quad (14)$$

Analysis of Capacitive DLTS signals is complicated by the fact that the charges observed within the MIS structure exist in series, resulting in capacitances in series rather than in parallel. This effect can be used to great advantage in some measurements, however. Of the charges defined for the MIS structure, all but the charges at the interface and within the semiconductor can be ignored because these charges are defined by the material and not by the voltage applied across the MIS structure, implying that no capacitance results from these charges.

The traditional model of the steady state capacitances existing in an MIS capacitor calls for two separate capacitors in series. The capacitance closest to the gate electrode is that of the insulating layer and is the direct result of the charge that is "piled up" at the interface as well as in the depletion layer when a high-frequency Alternating Current signal is applied. This capacitance may be expressed either as the permittivity of the insulator (ϵ_i) divided by the thickness of the insulator (t_i) or as the charge within the semiconducting film divided by the voltage present across the insulator V_i. Bearing in mind that this insulator voltage may be re-expressed as the difference between the voltage applied to the gate electrode (V_G) and the sum of the surface potential and the workfunction mismatch between the electrode and the semiconductor, the following equation may be derived.

$$C_I = \frac{\varepsilon_i}{t_i} = \frac{Q_D + Q_{IS} + Q_B}{V_G - \phi_S - \phi_{MS}} \quad (15)$$

The second capacitance is due to the depletion layer. Specifically, because the ionized dopant atoms of the depletion region form a charged layer with defined width as opposed to a "sheet of charge", a series capacitance results. This capacitance is simply defined as the permittivity of the semiconductor (ϵ_s) divided by the length of the depletion layer (W), which is defined using (2).

$$C_{dep} = \frac{\varepsilon_s}{W} \quad (16)$$

Because the two following capacitances exist in series, the following effective capacitance may be derived [24].

$$C_{eff} = \frac{(C_I)C_{dep}}{C_I + C_{dep}} \quad (17)$$

In a transient scenario, the steady-state model is further complicated by the emission of carriers from filled traps. From the steady-state analysis above, it is trivial to demonstrate that while the depletion capacitance is only affected by the emission of bulk trap states, the insulator capacitance is actually dominated by emission of both bulk and interface states.

When bulk states exist at low levels in comparison to the total charge present within the MIS structure, the transient decay of bulk states can be ignored when considering the behavior of the oxide capacitance over time. This is not the case for interface states, which typically make up

the majority of the observed trap states within an MIS structure. When the voltage is pulsed, free carriers will shift rapidly to maintain the capacitance of the oxide. Interface states and bulk states rely on thermal emission to generate free carriers and return to equilibrium. Prior to the formation of steady-state conditions, excess interface state charge will still contribute to the insulator capacitance, resulting in an observed transient capacitance which is higher than that at steady state. Thus, the insulator capacitance can be considered as made up of the steady state capacitance and a transient pseudo-capacitance which exists in parallel and represents the emission from interface states. This pseudo capacitance is the difference between the transient concentration of interface states and the steady-state concentration of interface states divided by the voltage applied across the insulator. The insulator capacitance may be defined as follows.

$$C_I = \frac{\varepsilon_i}{t_i} - \frac{Q_{IS}(t) - Q_{IS}(t=\infty)}{V_G - \phi_S - \phi_{MS}} \quad (18)$$

This insulator capacitance may be converted into a differential capacitance by eliminating all steady state contributions and by differentiating the interface-state concentration.

$$\Delta C_I = \frac{-\Delta Q_{IS}}{V_G - \phi_S - \phi_{MS}} \quad (19)$$

In the case of the depletion capacitance, the capacitance itself may be simplified using a Taylor Expansion about the doping of the semiconductor, N_A, where all but the first two terms of the series are neglected. The resulting approximation is as follows [25].

$$C_{dep} = \left[N_A + 2(N_T - Q_B(t)/W_i)\right] \times \left(\frac{\varepsilon_s q}{2\phi_s}\right)^{1/2} \quad (20)$$

This depletion capacitance may be converted into a differential capacitance by neglecting the effect of N_A due to it being a steady state component and by differentiating the bulk trap state contribution, which is time dependant [25].

$$\Delta C_{dep} = \frac{-2\Delta Q_B}{W_i}\left(\frac{\varepsilon_s q}{2\phi_s}\right)^{1/2} \quad (21)$$

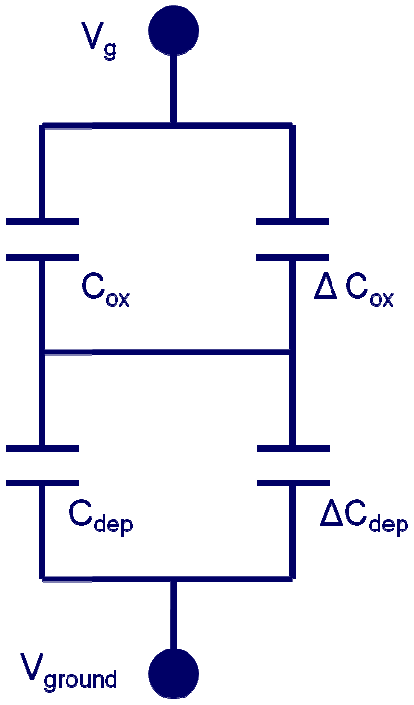

Figure 2: The Small Signal Model for DLTS of a MOS Capacitor – The oxide capacitance is modified to include the transient capacitance due to interface states while the depletion capacitance is modified to include the effects of transient bulk states on the depletion capacitance. The effects of bulk trapping may be separated from the effects of doping by perfoming a Taylor Expansion.

An expression for the differential effective capacitance may be extracted using the quotient rule. In this extraction, it is assumed that either no interface states exist, leading to a constant effective insulator capacitance, or that no bulk states exist, leading to a constant depletion capacitance. In making this assumption, two separate expressions for the change in effective capacitance with time may be derived as follows.

$$\Delta C_{eff}\left(Q_{is}=0\right)=\frac{dC_{eff}}{dC_{dep}}\frac{dC_{dep}}{dt}\Delta t \quad (22\text{-}1)$$

$$\Delta C_{eff}\left(Q_{D}=0\right)=\frac{dC_{eff}}{dC_{I}}\frac{dC_{I}}{dt}\Delta t \quad (22\text{-}2)$$

The change in the insulator capacitance as well as in the depletion capacitance with respect to time may be related back to the DLTS charge transient when they are multiplied by the change in time. By assuming only small variations in capacitance occur over time for C_I and C_{dep}, a simple expression may be derived for the change in C_{eff} with respect to its constituent capacitances at steady state. The product of this expression and the differential insulator and bulk capacitances may be expressed as follows.

$$\Delta C_{eff} = -\left(\frac{\varepsilon_S q}{2\phi_S}\right)^{1/2}\left(\frac{C_I^2}{\left(C_I + C_{dep}\right)^2}\right)\frac{2\Delta Q_B}{W} \quad (23\text{-}1)$$

$$\Delta C_{eff} = -\frac{C_{dep}^2}{\left(C_I + C_{dep}\right)^2}\frac{\Delta Q_{IS}}{V_G - \phi_S - \phi_{MS}} \quad (23\text{-}2)$$

This yields an approximate expression for the DLTS response of a capacitive signal. It is useful to note that it is not difficult to extract the quasi-static depletion and insulator capacitances, represented by C_{dep} and C_I. These terms may be easily derived from the Capacitance-Voltage characteristics of any MISCAP prior to DLTS measurements. This analysis is required for the measurements on a MISCAP to take place in order to determine the precise voltages required to generate the surface potentials desired for testing.

In the case of the measurement of insulator states on a thick insulating layer, where C_I is much smaller than C_{dep}, or where bulk states are being measured on a thin insulator or highly resistive substrate, where C_{dep} is much smaller than C_I, the derivative of C_{eff} with respect to its

constituent capacitances may be ignored and the resulting change in C_{eff} with respect to time is equal to the change in C_{dep} or C_I with respect to time.

In the case of a near-perfect semiconductor crystal, the effects of bulk trap states can be neglected as they will be inconsequential in comparison to the states arising at the interface. It is obvious that no structure can actually exist with zero interface states, but in the case where the insulator capacitance is sufficiently large in comparison to the depletion capacitance, interface states may be taken to be non-existent and the effect of trap states alone may be considered.

In the case of a capacitive measurement where interface states are assumed negligible and only the depletion capacitance is assumed variable, dividing by (23-1) by (20) results in a greatly simplified expression for Ceff, where W is the depletion width during the emission pulse.

$$\frac{\Delta C_{eff}}{C_{dep}} = -\left(\frac{C_I^2}{\left(C_I + C_{dep}\right)^2}\right)\frac{2\Delta Q_B}{WN_A} \quad (24)$$

To a first order, the differential effective capacitance arising from a combination of interface states and bulk trap states may be approximated by a summation the equations corresponding to the DLTS signal caused by interface states in the absence of bulk states and bulk states in the absence of interface states. From this summation, it is readily apparent that the signals arising from interface states or bulk trap states with set magnitudes may be attenuated or amplified with respect to one another by varying the corresponding insulator or depletion thicknesses. This effect has been touched on previously. Wang noted that the signals observed from bulk trap states could be amplified in capacitive DLTS measurements performed on the gate of a

MOSFET by biasing this MOSFET such that the channel region was in a state of deep depletion [26].

In the case of a MIS Capacitor, this same effect may be produced for small depletion widths by increasing the insulator capacitance, or decreasing the insulator thickness. In the case of large insulator thicknesses, reducing the depletion capacitance to a small value by increasing the resistivity of the semiconductor or by biasing into deep depletion accomplishes the same effect. This is not a counter-intuitive effect when the series nature of the insulator and depletion capacitances is considered. The increase of the insulator capacitance relative to the depletion capacitance necessitates that more interface charge is required in order to maintain the same shift in effective capacitance observed in DLTS because the low capacitance always dominates in a series combination. Because this charge is fixed by the presence of interface states, the signal due to interface states must necessarily attenuate, eventually becoming negligible in comparison to the bulk state signal.

This effect is observed in simulations of DLTS transients with variable oxide thickness and substrate resistivity. These simulations were performed by converting (5-1) and (7-1) into Riemann Sums for bulk traps with a set activation energy, capture cross section and trap density and for interface states with a set state density and capture cross-section. The variation in surface potential was defined in order to determine the change in depletion width as well as the energy range of interface state emission. The machine settings for a DLTS system, specifically t_1, t_2 and t_D as well as the range of the temperature sweep were set for the simulation. Once the variation in charge density between t_1t_D and t_2t_D was calculated for the interface as well as the bulk, the insulator capacitances and depletion capacitances were calculated and set in parallel to simulate a capacitive DLTS signal.

Increasing insulator capacitances or decreasing depletion capacitances attenuate the DLTS signal corresponding to interface states, leaving only the signal associated with bulk trap states in the semiconductor. The effects of increasing insulator capacitance can be observed in Figure 3, where a decreasing insulator thickness forces a transition in the DLTS signal from an extended energetic band for thick insulators (corresponding to the interface state signal) to a signal due to bulk trap states with discrete energies for thin insulators. The effects for increasing substrate resistivity can be observed in Figure 4, where an increasing substrate resistivity forces a transition in the DLTS signal from an extended energetic band for highly conductive substrates (corresponding to the interface state signal) to a signal due to bulk trap states with discrete energies for highly resistive substrates.

It should be noted that the linear summation of DLTS signals arising from interface states and bulk states is a reasonable approximation, but is not valid as the signals from either source become large in comparison to their constituent steady-state capacitances because of non-linear effects generated by the series combination of capacitances.

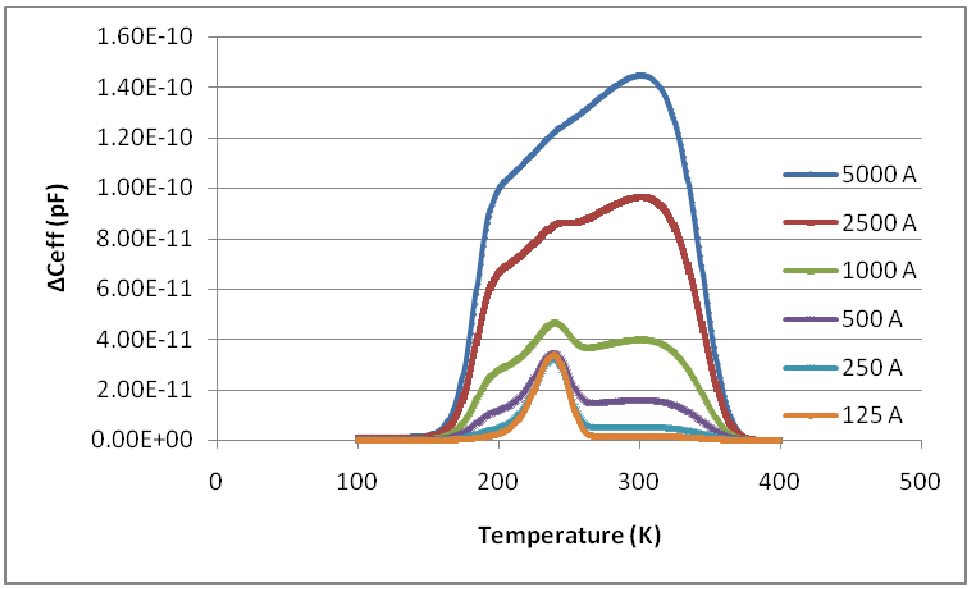

Figure 3: Variable DLTS signals due to interface and bulk states with respect to insulator thickness – This simulation was performed for a sample with a hole carrier concentration equal to $1x10^{15}$ cm^{-3}, a t_D value of $1x10^{-4}$s and a bulk trap energy of E_V+.3eV with a voltage across the insulator equal to 1V and with an interface state density of $2x10^{10}$ /eV-cm^3.

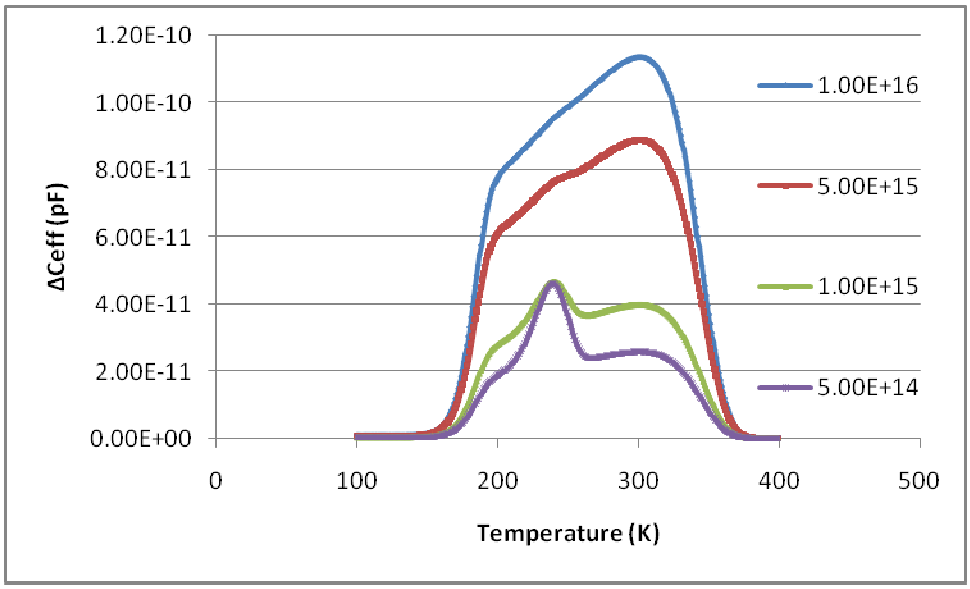

Figure 4: Variable DLTS signals due to interface and bulk states with respect to bulk resistivity – This simulation was performed for a sample with an insulator thickness equal to 1000Å, a t_D value of $1x10^{-4}$s and a bulk trap energy of E_V+.3eV with a voltage across the insulator equal to 1V and with an interface state density of $2x10^{10}$ /eV-cm^3.

The effect of interface state attenuation may also be experimentally verified. An Si sample with resistivity in the range of 8Ω-cm to 15Ω-cm was cleaned and scribed. This samples were oxidized in a Bruce 7670 thermal oxidation furnace. This was a dry oxidation consisting of an initial ramp-up in nitrogen from 800°C to 900°C at a ramp rate of 10°C per minute followed by a 40 minute soak in ambient oxygen. Following this soak step, the temperature was decreased from 900°C to 800°C at a cool down rate of 5°C per minute. This resulted in the growth of a dry oxide to an average thickness and standard deviation of 191.38Å and 3.636Å, respectively, over the surface of the sample.

The sample was implanted with phosphorus to act as a baseline for DLTS measurements. The sample was implanted with the phosphorus isotope, P31, at an energy of 60KeV, a tilt of 7 degrees, a rotation of 45 degrees and a fluence of $2x10^{11}$ P^{31}/cm^2. Following ion implantation, photoresist was spun on the front-side of each wafer and hard-baked at a temperature of 150 °C. The backsides of both samples were etched in a 10:1 Buffered Oxide Etchant (BOE) and the photoresist covering the front of each sample was stripped in solvent and rinsed.

The sample was cleaved in half. Half of the sample was annealed at 450°C for 30 minutes while the other half of each sample was not annealed in order to preserve the states present in the bulk following ion implantation. Metallization was performed on the front and back sides of both samples in a CVC Evaporator Glass Jar. Approximately 200nm of aluminum was blanket deposited on the backside of each sample. A similar deposition of the same approximate aluminum thickness was performed on the front side through a shadow mask with circular features ranging from 1mm to 5mm in diameter.

MIS devices with diameters of 1mm were cleaved from each sample and were analyzed using DLTS in a SULA DLTS system. The steady state capacitance of the sample was analyzed from 5V to -5V. The capacitance-voltage response was used to define a square wave pulse for DLTS analysis that biased each sample from a state of shallow depletion, with the surface potential approaching the flat band condition, to deep depletion, with the surface potential approaching inversion. The sample was cooled to 100K and heated to 400K with measurements of the capacitance transient taken every 0.25K as heating occurred. These transients were analyzed using a boxcar integration technique with windows defined at t_2=7 and t_1=2.3 times $t_{D,}$ where t_D is equal to the machine-defined variable time delay ranging from 5 ms to 0.1 ms, thus varying the values of t_1t_D and t_2t_D and changing the temperature positions of trap signals observed in DLTS spectra and allowing an Arrhenius Plot to be generated. The resulting spectra were analyzed assuming a single-exponential dependency, meaning that any convolved peaks were analyzed as though they were a single peak.

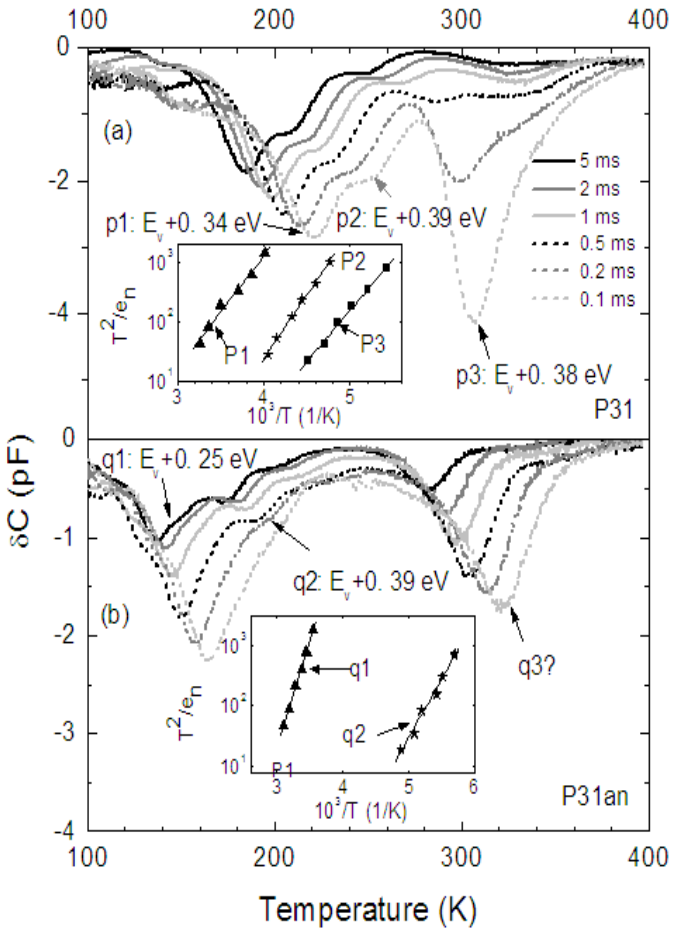

Figure 5: DLTS Spectra of a p-type silicon sample implanted with the P^{31} isotope of Phosphorus – Analysis indicates a small baseline signal superimposed with each bulk signal. This underlying base signal acts as a near-constant offset and likely corresponds to the interface signal. The high quality of observed trap signals as well as the lack of signal variation with voltage (not shown) indicates bulk trapping. The DLTS spectrum in Figure 5a corresponds to the unannealed sample while the DLTS spectrum in Figure 5b corresponds to the annealed sample. DLTS analysis biased each sample from a state of shallow depletion, with the surface potential approaching the flat band condition, to deep depletion, with the surface potential approaching inversion. (Plot Courtesy of J. Senawiratne, Corning Inc.)

Analysis of the resulting Deep Level Transient Spectra demonstrated a similar attenuation effect as that predicted in the simulated results. A baseline signal, equal to roughly .2pF and extending from 100K to 350K and attenuating to roughly zero at elevated temperatures is evident in the sample which was implanted and annealed (Figure 5b). The baseline of the measurement was small with respect to bulk state signals, a situation indicative of a thin

insulating barrier between the metal electrode of the MIS Capacitor and the semiconductor. The states observed during DLTS testing have maximum values of 4pF in the unannealed sample (Figure 5a). These states as well as the baseline signal cannot be attributed to interface states as capacitive signal associated with these states corresponds to an interface state density of the same order of magnitude as $1x10^9$ /cm^2 at the insulator thickness generated by the oxidation procedure. This was derived using (23-2).

Another readily apparent effect of the thin insulator thickness is the high quality Arrhenius fit of all bulk states observed by the MIS Capacitor. This is indicative of minimal distortion due to underlying signals caused by the interface which would corrupt the measurement of activation energy and capture cross section. Lastly, the lack of variation with changing emission and capture potentials is also indicative of the lack of interface states. A changing potential setting associated with DLTS would shift the interface state signal to reflect the new maximum and minimum band position of the scan and, as a result, the observable spectrum would shift. Moreover, the quality and calculated values of Arrhenius Plots would shift with this shifting voltage as distortion effects changed. This was not the case.

3.3: A Spectral Fitting Program

It is a common occurrence for peaks of similar energies to superimpose on one another during the temperature scanning associated with DLTS. Without the aid of some computer program to assist in spectral fitting, the separation of these peaks is difficult, at best. In many cases, two peaks will superimpose such that they appear to form a single peak with an unusually

broad temperature signature. Spectral fitting provides a means of eliminating the subjectivity of manual peak identification from the process of spectral analysis.

By utilizing the equations derived for the spectral response of a single-sided junction as expressed in Chapter 3, a simplistic program may be generated in order to perform spectral fitting. Initially, a DLTS spectrum may be input into the program and the noise associated with the measurement may be eliminated by use of a running average or another advanced technique such as a Fast Fourier Transform followed by filtering. In the case of the program created, this smoothing effect is accomplished by means of a running average. A granularity is specified by the user, who defines the number of data points to be averaged together. By means of a Do-While Loop, the program averages each group of points corresponding to the user's selection and assigns them to the temperature of the first point in the group, creating a smoothed spectrum.

This smoothed spectrum is input into a Peak-Finder subroutine, which identifies peak maxima and derives activation energies, capture cross-sections and trap densities based off of a mono-exponential model (i.e. a single trap model). This is accomplished by a second Do-While Loop which searches for points which are greater than corresponding points to either side of their position. The program may only find one peak maximum at a time. The activity of this Do-While Loop is modified by the user, who may specify a starting temperature for which the search for a peak maximum may begin, the minimum magnitude of the peak maximum and the spread of points to either side of the point being analyzed at each iteration of the Do-While loop to determine the maximum position. This derivation may be performed through the use of an Arrhenius Plot as was developed by Lang, or with a fit based on the Half-Width at variable amplitude, which will be derived. In the case of the Half-Width method, the user may also specify the number of points to either side of the maximum to be analyzed for Half-Width

calculations, the maximum and minimum magnitudes of the DLTS signal to be analyzed for Half Width as well as specifying whether the “right” or “left” side of the peak is to be analyzed.

The resulting Arrhenius of Half Width Analyses yield expressions for the Activation Energy, Capture Cross Section and Trap Density associated with a given peak. After the user specifies which fits appear reasonable, the program uses the equations for the spectral response of a single sided junction to eliminate those peaks which the user has indicated as properly identified, leaving any signals missed by the sub-routine. This is achieved by inputting the computer-calculated Activation Energy, Capture Cross Section and Trap Density into a subroutine which generates a theoretical peak from the computer-specified constants for a given temperature sweep and subtracts the theoretical peak from the experimental data.

This procedure is repeated until all peaks have been identified in the input spectrum and subtracted out. At this point, the program re-fits the spectrum by varying all activation energies, trap densities and capture cross-sections, and analyzing the total squared error between the spectral fit and the input DLTS spectrum as all identified trap characteristics are varied. The resulting settings which result in the lowest total squared error are taken to be the true trap Activation Energies, Capture Cross-Sections and Trap Densities for the measurement and are output by the program.

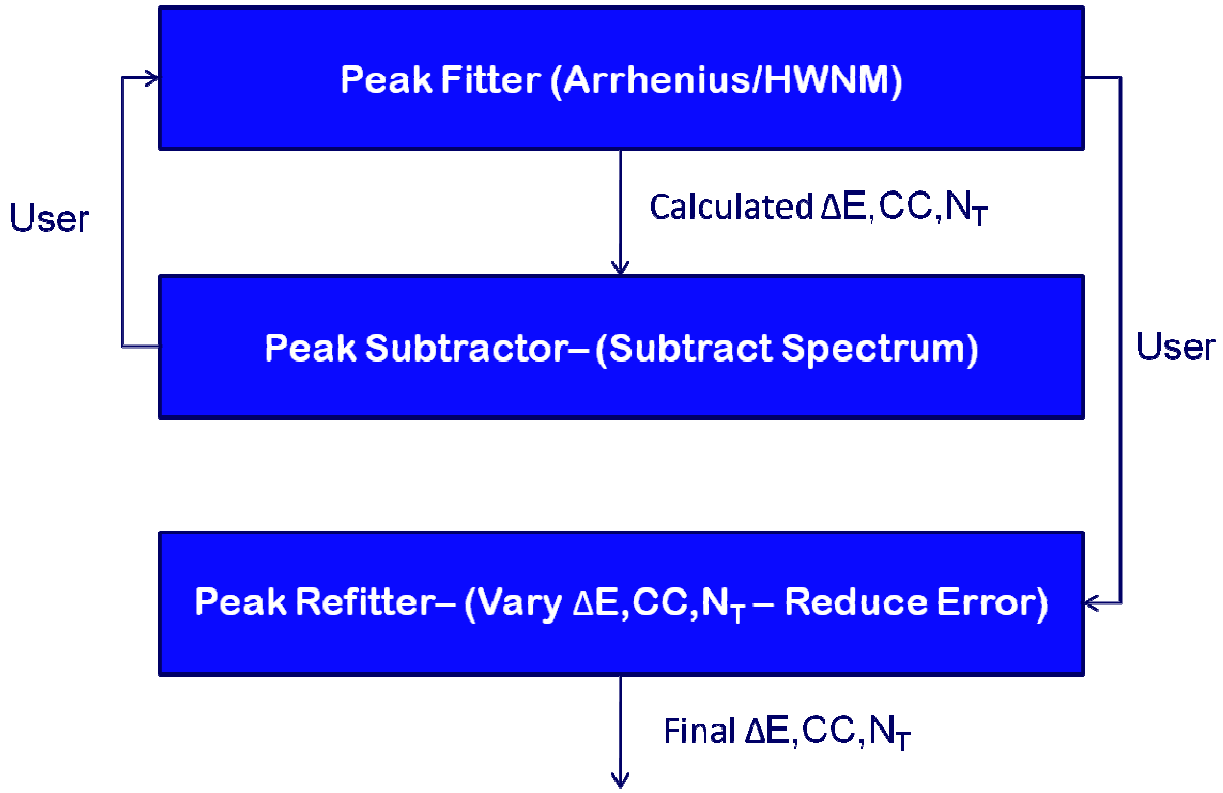

Figure 6: Program Design for Semi-Automated Fitting – Input spectra undergo "fitting" where the signals are smoothed, maxima are identified and the activation energy, trap density and capture cross-section are calculated given the position and shape of the signal with respect to machine constants. A theoretical peak with the same constants is subtracted and the process is continued until all peaks are subtracted from the signal. At the user's discretion, the extracted peak values may be input into a "re-fitter" to give the constants which yield the lowest error between the theoretical and experimental signals.

3.4: The Half Width at "N^{th}" Maximum

The measurement of traps arising from analysis via Deep Level Transient Spectroscopy utilizing a Boxcar Correlator has traditionally been achieved through the use of an Arrhenius Plotting method. This DLTS method makes use of multiple boxcar correlators to measure trap signals over multiple sampling windows in a single temperature sweep or, in some cases, over several temperature sweeps - each of which make use of different correlator settings by alteration of the delay time, t_D. An Arrhenius Plot may be generated by measuring the resulting positions

in temperature space of each peak maximum and tracking the change in this position with changing correlator settings. The changing correlator settings associated with the changing sampling window define a characteristic emission rate, e_{PM}. The relationship between these variables and the characteristic emission rate defined by the window is derived by solving for the derivative of a DLTS signal with respect to emission rate and setting this derivative equal to zero in order to extract the emission rate at the DLTS peak maximum, as follows [4].

$$e_{PM} = \ln\left(\frac{t_2}{t_1}\right) / [t_D(t_2 - t_1)] \quad (25)$$

By plotting the natural logarithm of the quotient of the emission rate, e_T, and the square of the maximum temperature with respect to the inverse product of the maximum temperature and Boltzmann's Constant, an Arrhenius Plot may be generated which yields a linear function. The slope of this function yields the activation energy of the trap analyzed while the intercept with the $\ln(e_T/ T_M^2)$ axis yields the a function from which the capture cross section may be extracted as shown in Figure 5 in Chapter 1.

This is an accurate means of deriving the characteristics of a deep level trap when no other DLTS signals are close enough to superimpose on the maximum of the peak. The method is, however, inefficient, only making use of a single data point per peak extracted by the temperature scan associated with DLTS. Furthermore, this method is expensive, requiring a substantial investment of time and capital. Generating an Arrhenius Plot from a DLTS spectrum using only one or a few correlators is time-consuming, requiring multiple temperature sweeps

which may require days to complete. The alternative solution to a substantial time investment is the purchasing of a large number of correlators, an expensive proposition. Lastly, Arrhenius plots are very susceptible to distortion effects from superpositioning of peaks due to the assumption of single-rate decay. Arrhenius plots provide little means of avoiding this distortion effect because the peak maximum alone must be used.

An alternative to the Arrhenius Plot does exist. D.V. Lang has proposed a means of measuring the Activation Energy of a trap from the Full Width at Half Maximum of a DLTS spectrum derived from DLTS measurements made with a Lock-In Amplifier [27]. A similar derivation is performed in this text for the Half Width at "Nth" Maximum, where N is equal to the ratio between the magnitude of a DLTS signal at any point along the curve of a DLTS peak and the magnitude of the peak at its maximum. This novel derivation provides the means of using the entire curve of a DLTS peak to extract the activation energy and the capture cross section of a deep level trap, enabling faster accurate signal identification. Additionally, the method described below may offer more versatility because a half-width measurement can be used to avoid superimposed signals on the opposite side of a DLTS peak from the side on which the measurement is taking place.

As demonstrated previously, the emission rate for a given trap is dependent upon a variety of constants, including the activation energy, the capture cross section, the density of states and the thermal velocity. The only variable which the emission rate is dependent upon for a given trap state is the temperature at which the measurement is being made. Thus, a DLTS peak may be transformed from temperature space to emission rate space and back again at will and two points on a DLTS curve may be defined by an emission rate just as easily as they might be defined by

the temperature. The emission rate at any point along a DLTS curve, e_{PN}, may be related to the emission rate at the point at which the maximum occurs, e_{PM}, by some constant, k_O.

$$e_{PN} = k_O e_{PM} \quad (26)$$

The emission rates along the curve and at the peak maximum may be related to their constituent temperatures, T_N and T_M. This is accomplished by using the definition of the emission rate as expressed in Chapter 1, where σ represents the capture cross-section of the trap, γT^2 represents the product of the density of states in the majority carrier band multiplied by the thermal velocity of the majority carrier, ΔE is the energy jump between the trap energy and the majority carrier band and k is Boltzmann's Constant.

$$\sigma\gamma T_N^2 e^{-\Delta E/kT_N} = k_O \sigma\gamma T_M^2 e^{-\Delta E/kT_M} \quad (27)$$

Because for a single trap species which traps the same majority carrier, the capture cross section, thermal velocity and density of states are equal along the entirety of the curve, σ and γ may be eliminated from the equation. The squared temperature terms may be separated from their corresponding exponential terms and the natural logarithm taken of both sides of the equation. After some algebraic manipulation, the following equation results for the activation energy. The form of this equation is critical as it demonstrates a means of measuring the

activation energy of a DLTS peak which has no dependence on capture cross-section. This facilitates the calculation of trapping characteristics because no iterative solution is required to extract important parameters.

$$\Delta E = \frac{k\ln(k_O T_M^2/T_N^2)}{(1/kT_M - 1/kT_N)} \quad (28)$$

Assuming k_O may be calculated, an expression exists for the activation energy. The resulting value of the activation energy may be input into the expression for the emission rate at the maximum of the peaked DLTS function. Because the value of this emission rate is also defined for the maximum of the DLTS peak through the machine constants t_1 and t_2 as well as the delay time, t_D, a value for the capture cross-section may be derived by equating the machine-defined emission rate at the maximum to the definition of the emission rate at the maximum defined by the maximum temperature, and solving for the capture cross section, σ.

$$\sigma = \frac{\ln\left(\frac{t_2}{t_1}\right)/[t_D(t_2 - t_1)]}{\gamma T_M^2 e^{-\Delta E/kT_M}} \quad (29)$$

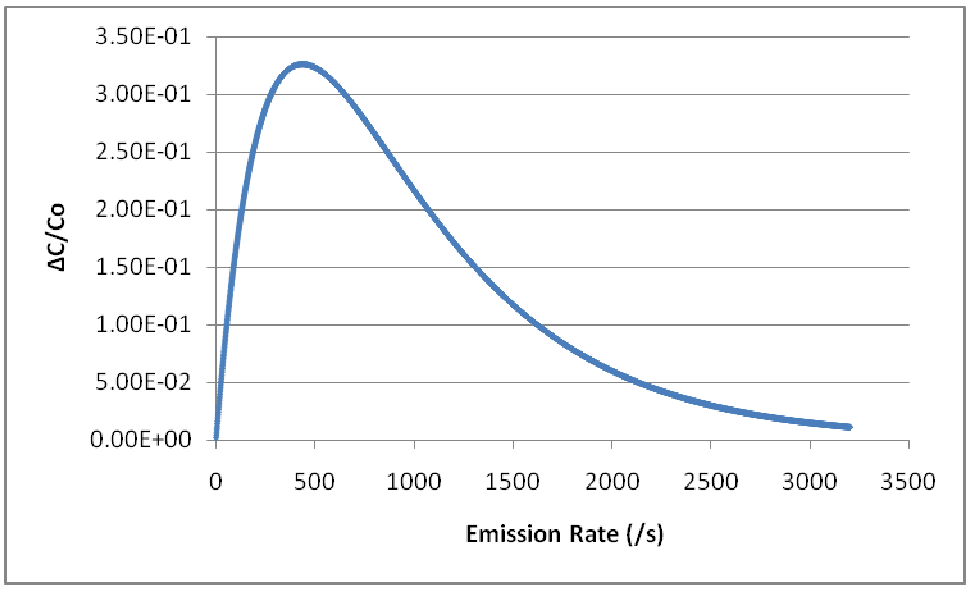

Figure 7: Variation of ΔC/Co with respect to the Emission Rate (s^{-1}) for a generic DLTS signal – The machine settings for this particular measurement were a value of 2.8 for t_1, 7 for t_2, and $5x10^{-4}$ s for t_D.

No expression yet exists for the constant, ko, which relates the two emission rates. In order to solve for this constant, the equation for the curve shape of a DLTS peak must be transformed from temperature space to emission space, as described earlier. As also was stated earlier, the expression for the DLTS peak as a function of the emission rate may be differentiated to yield the expression in (3) for the emission rate at the peak maximum, which is, again, a function of the two machine constants, t_1 and t_2 as well as the delay time, t_D. The emission rate along the curve may be related to the emission rate at the maximum through k_o, as before. By substituting this known pair of emission rates into the definition of a DLTS peak, a complete expression may be derived for the peak magnitude at both points. By deriving the magnitude of the point along the curve of the DLTS peak by the magnitude of the maximum, an expression for N in terms of t_1, t_2, t_D and k_O may be derived. Because all of these variables are known with the

exception of k_O, this serves as an ad-hoc derivation for k_O, which is obviously dependent upon the rate window as well as the point on the curve being sampled.

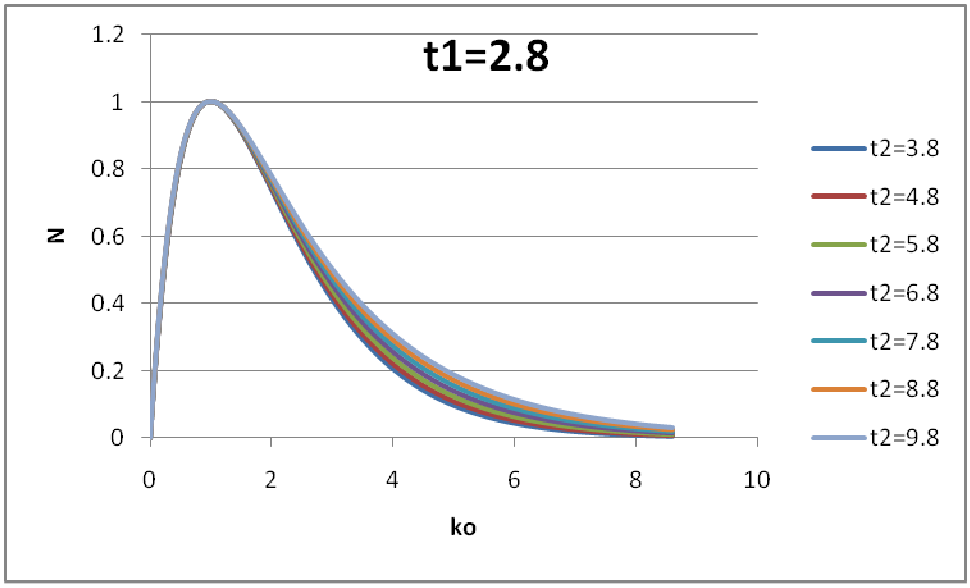

Figure 8: The variation the scaling constant, k_O, for variable "N" and variable t_2 settings.

$$N = \frac{(t_2/t_1)^{-k_O t_2/(t_2-t_1)} - (t_2/t_1)^{-k_O t_1/(t_2-t_1)}}{(t_2/t_1)^{-t_2/(t_2-t_1)} - (t_2/t_1)^{-t_1/(t_2-t_1)}} \quad (30)$$

The resulting function is peaked at the point where both N and k_O are equal to one, this point being the maximum of the DLTS peak. The left hand side of the function shown in Figure 7 and Figure 8 corresponds to the left hand curve of the DLTS peak, and it attenuates rapidly, reaching the point where both N and k_O are equal to zero. On the right hand side, the function attenuates slowly, only approaching a value of N equal to zero as k_O approaches an infinite

value. As is readily observable, the left hand side of the function does not vary strongly with varying values of the machine constants t_1 and t_2, tending toward the expression derived from the derivative of the exponential decay function (that being the point where t_1 and t_2 are equal). This is not the case on the right hand side of the equation. As the values of t_1 and t_2 separate, the magnitude of the function rises quickly, diverging much more rapidly from the expression derived from the case of a perfect derivative.

The function provides a useful means for extracting the correct k_O value necessary for analysis of the activation energy in a situation where the peak is being fitted manually. In a computer program, however, the inherent delay associated with a programmed look up table necessitates the generation of two polynomial fitting functions relating an observed value of N to its corresponding value of k_O. This is accomplished by separating the function relating N to k_O at the point of the peak where N and k_O are equal to one, switching the dependant and independent variables of the resulting functions and fitting the resulting curves via a polynomial expansion. The result of this procedure is two separate polynomial functions, one representing the right hand side of the equation and the related DLTS peak and the other representing the left hand side of the equation and the related DLTS peak.

The polynomial function is an adequate first-order approximation, but the inherently sensitive nature of the measurement of activation energy means that any deviation from the theoretical function results in substantial noise inherent in the measurement. For a fit utilizing a sixth order polynomial expansion, the error associated with the measurement remains reasonably steady with the standard deviation of the activation energy, with the error at around 3% of the true value of the peak energy and rapidly increasing to 15% for low-energy, high capture cross section peaks. This error is magnified significantly for capture cross-section measurements

because of the fact that the activation energy and any error in the derivation for this energy are contained within an exponential term in the equation used for deriving the capture cross section. In the worst cases, associated with high energy and low capture cross section species, this variation can result in standard deviations exceeding an order of magnitude or more in capture cross-section. This effect is greatly reduced in cases where the standard deviation associated with the activation energy error steady at around 3% or less. In these cases, the standard deviation associated with the capture cross-section is less than an order of magnitude.

In order to verify the utility of the fitting function described above, an experiment was planned in which a MOS Capacitor was fabricated in the fashion described in Section 3.2. This MOS Capacitor was fabricated on a P-type Si sample with a resistivity in the range of 8 Ω-cm to 15 Ω-cm with an average insulator thickness and standard deviation of 197.19Å and 3.363Å, respectively, over the surface of the sample. The sample was implanted with the boron isotope, B11, at an energy of 45 keV, a tilt of 7 degrees, a rotation of 45 degrees and a fluence of $2x10^{11}$ B^{11}/cm^2 and was put through the same post-implant processing and biasing, analysis and heating conditions for DLTS as was described in Section 3.2.

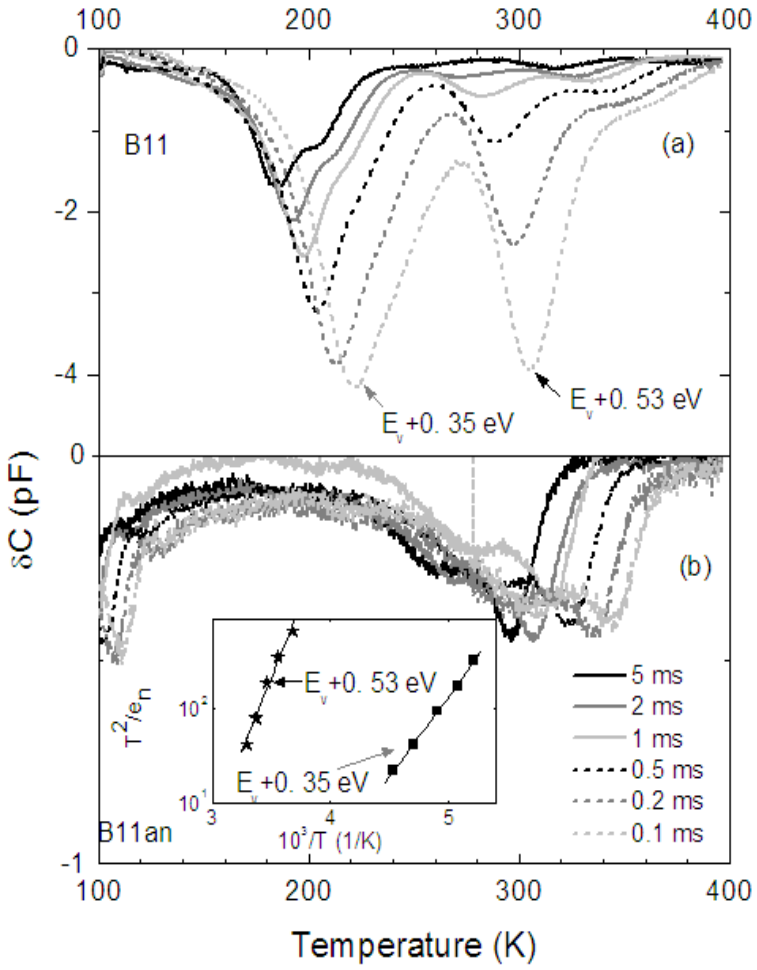

Figure 9: The DLTS Spectra of as-formed and annealed samples after B11 ion implantation. Figure 9a represents the DLTS signal resulting from analysis of the as-formed sample implanted with B11. Figure 9b results from the DLTS analysis of the annealed sample. Two peaks, one at low temperature and one at high temperature were observed. The low temperature peak contains a shoulder, indicating that it results from two separate deep level trap signals.

Analysis with HWNM fitting demonstrated the presence of two separate peaks in the peak-shoulder combination, which resulted in complete elimination of the combination observed. Analysis of the low-temperature peak in Figure 9a demonstrates the presence of a single dominant peak as well as a shoulder on this peak which belongs to a secondary convolved signal. One peak with an energy equal to approximately E_V+.27eV and a capture cross section equal to

approximately $5.8x10^{-18}$ cm^{-2} was observed in this peak-shoulder combination. This was not of the same approximate value as was extracted from the Arrhenius Plot identification, changing the identified peak from a carbon-oxygen interstitial bond to a divalency. This result is not surprising given that the presence of a secondary peak in this low-temperature signal would likely change the position of the observed peak maximum, also changing the results of the Arrhenius Plot. A secondary peak was observed with an energy equal to E_V+.38eV and a capture cross section of $7.06x10^{-16}$ cm^{-2}, which corresponds well with the carbon-oxygen interstitial bond. Lastly, a peak was observed at higher temperatures with an energy of E_V+.55eV and capture cross section of $2.78x10^{-15}$ cm^{-2}. This fit well with experimental measurements performed by Arrhenius Plotting, which is not surprising given that no significant shoulder is present in this high temperature peak. The successful analysis of the DLTS spectrum of the as-formed sample indicated that fitting via a HWNM method is a viable option. Furthermore, this analysis demonstrated several positive attributes of HWNM fitting beyond efficiency. Note that because of the high numbers of data points available for fitting, HWNM fitting procedures are highly sensitive to distortion. The range over which the measurement is made may be altered to avoid distortion effects.

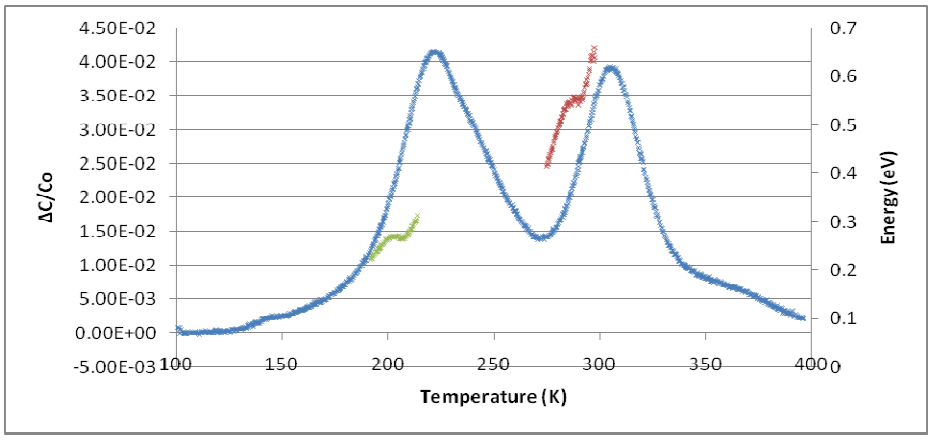

Figure 10: A sample spectrum from the as-formed B11 implanted sample. This spectrum was analyzed with the HWNM measurement and the energies of the two dominant peaks were extracted over the full range of their magnitudes, demonstrating distortion effects (non-constant extracted energies) which were avoided during the final fit. The DLTS signal is indicated by the single unbroken trend in the figure. The extracted energies of the dominant peaks in the low-temperature and high-temperature signals are given by the two broken lines.

Chapter 4: Molecular Hydrogen Ion Implantation Experiments

4.1: Kinetic Differential Analysis

In order to properly correlate structural defects to their corresponding electrical effects, an analysis of the dynamic annealing characteristics of all structural and electronic defect species is required. The simplest method for making this correlation is the analysis of the annealing kinetics of both structural and electronic defects with respect to temperature and time. It would seem reasonable to make the assumption that the electronic counterpart of a structural defect should possess the same kinetic characteristics associated with this genesis and destruction. That is, the reactions giving rise to and eliminating electronic defects should be the same as the reactions giving rise to and eliminating structural defects. Thus, there should be some correlation between the order of reaction for electronic and structural defects, their activation energies, and their associated rate constants.

The general method of analysis for an unknown system of reactions is a detailed analysis of the concentrations of reactants and products over a temperature and time range corresponding to the typical range of activity for the reaction system. Variations in temperature allow analysis of the thermodynamic characteristics of the reaction, including the activation energy and rate constants associated with the reaction. Variations in time allow for analysis of reaction order and the corresponding form of the reaction itself. These measurements require a substantial investment of capital as two separate dimensions of a design space must be fully characterized.

There is, however, a means of reducing the design space which must be investigated from two dimensions to one. The fundamentals of this technique will be discussed and a simple

experiment will be performed to act as a general proof of concept for the execution of this technique. In general, the kinetic characteristics of a chemical reaction may be specified in the expression for the reaction rate. This rate is the product of thermodynamic components (present in the reaction rate) and mechanistic components (present in the exponents appearing above the concentration terms).

The rate constant is ordered much like the rate associated with a DLTS spectrum. The rate constant may be expressed as a function of the thermodynamic order of the reaction (T^n) a "rate constant" v_O, which takes into account the steric hindrance factors and capture cross section associated with the reaction, and a Boltzmann statistic associated with the activation energy (ΔE) of the reaction. The mechanistic order of the reaction multiplies into the thermodynamic rate constant of the reaction. Regardless of whether the component being studied is a reactant or a product, the mechanistic order of the reaction is an expression of the products that feed into the reaction. The concentration of each reactant multiplies into the mechanistic factor of the reaction. For the following reaction mechanism, the reaction rate is as follows, where k is Boltzmann's Constant [30].

$$xA + yB \rightarrow A_xB_y \qquad (1)$$

$$\frac{d(A_xB_y)}{dt} = v_0 T^n \exp\left(-\Delta E/kT\right) A^x B^y \quad (2)$$

Because the reaction rate and its associated kinetics are reliant on a collision model, it is unusual to see any reaction with a mechanistic order where the exponents add up to anything past

two, and no experimental evidence exists for a mechanistic order greater than three present in nature. In many cases, one reactant will exist in much larger concentrations in a system than the other reactant. In this case, the reaction kinetics are dominated by the most dilute reactant. This is the case in situations such as Ion Implantation, where the number of implanted reactants is typically much larger than individual defect species generated by high-energy ballistic injection. In general, when a reaction of unknown mechanism is being considered in a solid system, the reaction rate above may be simplified to the following expression, where the N_T is the concentration of the reactant or product being analyzed and m is the mechanistic order of the reaction. It should be noted that the thermodynamic order, n, is no longer present in the equation. The effects of this thermodynamic order are largely negligible in a solid system. It is from this expression that the method is derived.

$$\frac{dN_T}{dt} = v_O N_T{}^m \exp\left(-\Delta E/kT\right) \qquad (3\text{-}1)$$

$$\frac{dN_T}{dt} = v_O (N_O + N_{TO} - N_T)^m \exp\left(-\Delta E/kT\right) \qquad (3\text{-}2)$$

In the above derivation, the (3-1) represents the differential associated with a decay reaction. In the case of the generation reaction (expressed in (3-2)), some reactant with initial concentration N_O decays to form N_T. Thus, the rate may be expressed as a function of the remaining reactant concentration, which is simply the difference between the initial reactant concentration and the difference between the product concentration at any point during the reaction, N_T and at the onset of the anneal, N_{TO}. The overall method functions by comparing the

concentrations of constituent reactants and products in an as-formed sample (representing the initial conditions of the reaction) and comparing them to samples annealed for a short period of time. The change in reactant and product concentrations between the as-formed sample and samples annealed at variable temperatures constitutes a discrete differential of the reaction kinetics as a function of time, which may be approximated by the reaction rate because it is, itself, a perfect differential of these kinetics with respect to time. The first step to deriving this discrete differential is defining the resulting integral of an arbitrary reaction of n^{th} order, reaction velocity v_o, anneal temperature T, anneal time t, and activation energy ΔE. This is accomplished by performing the indefinite integral of (3-1) and (3-2) [31].

$$\frac{N_T}{N_O} = \left(1 + (n-1)t\frac{v_O}{N_O^{1-n}}\exp\left(-\Delta E/kT\right)\right)^{\frac{1}{1-n}} \quad (4\text{-}1)$$

$$\frac{N_O + N_{TO} - N_T}{N_O + N_{TO}} = \left(1 - (n-1)t\frac{v_O}{(N_O + N_{TO})^{1-n}}\exp\left(-\Delta E/kT\right)\right)^{\frac{1}{1-n}} \quad (4\text{-}2)$$

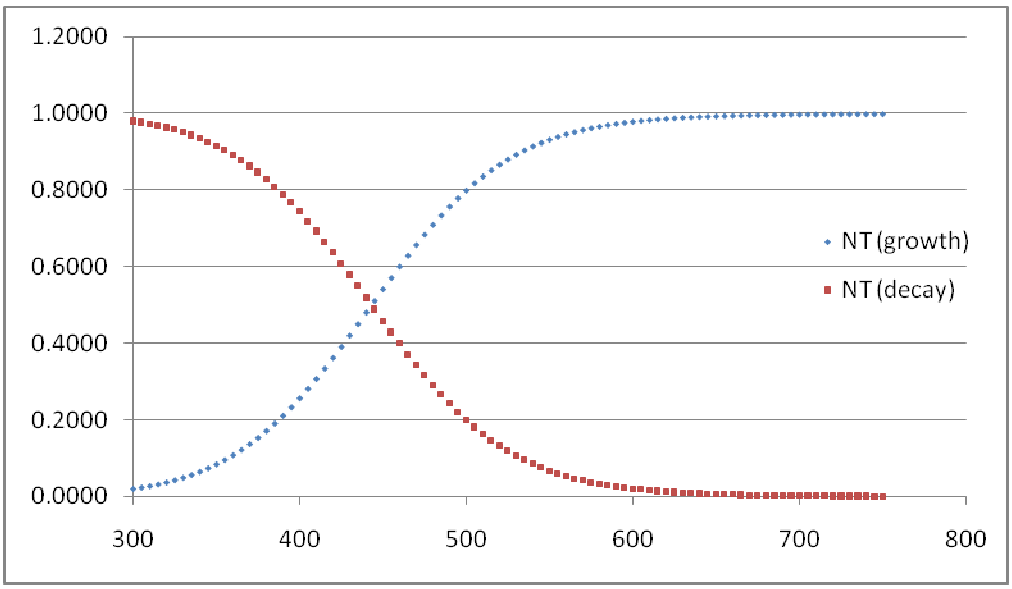

Figure 1: Variations in N_T/N_{TO} with respect to temperature for a generation reaction and decay reaction. This particular plot was generated for a reaction with a reaction order equal to 1.5, an activation energy equal to 1eV and a normalized reaction velocity equal to $4.5x10^6$ ($cm^{-3}s^{-1}$).

As before, the first term represents a decay reaction while the second equation represents a generation reaction. The natural logarithm of the rate expressed in (4-1) and (4-2) may be approximated by the second term and its associated sign alone multiplied by the inverse of (1-n) if this second term is much smaller than one. This is accomplished by making use of a Taylor expansion of the natural logarithm. In the case of a generation reaction (3-2), the resulting natural logarithm is positive. For a decay reaction (3-1), the natural logarithm is multiplied by -1.

$$\ln\left(\frac{N_T}{N_O}\right) \cong -t\frac{v_O}{N_O^{4-n}}\exp\left(-\Delta E/kT\right) \qquad (5\text{-}1)$$

$$\ln\left(\frac{N_O+N_{TO}-N_T}{N_O+N_{TO}}\right) \cong t\frac{v_O}{N_O^{4-n}}\exp\left(-\Delta E/kT\right) \quad (5\text{-}2)$$

By evaluating the ratio of natural logarithms of the concentrations observed if two separate samples are annealed for the same time but different temperatures, an expression may be derived which yields the Activation Enthalpy [32]. This may be achieved because the anneal time, reaction velocity and initial reactant concentrations are constant irrespective of the anneal temperature. The natural logarithm of the ratio of the natural logarithmic concentration at two separate temperatures, T_1 and T_2, multiplied by the Boltzmann Constant and the inverse of the difference between the second and the first inverse temperatures is taken and the result is as follows.

$$\Delta H \cong k\left[\frac{1}{T_2}-\frac{1}{T_1}\right]^{-1} \ln\frac{\ln(N_{T_1}/N_0)}{\ln(N_{T_2}/N_0)} \qquad (6\text{-}1)$$

$$\Delta H \cong k\left[\frac{1}{T_2}-\frac{1}{T_1}\right]^{-1} \ln\frac{\ln([N_0+N_{T0}-N_{T_1}]/[N_0+N_{T0}])}{\ln([N_0+N_{T0}-N_{T_2}]/[N_0+N_{T0}])} \qquad (6\text{-}2)$$

If the equations for the concentration variation with respect to temperature and time are further explored, a second equation may be expressed to derive the reaction velocity. This is accomplished by taking the natural logarithm of the ratio of the reactant concentrations observed at the two separate temperatures. The resulting derivation is as follows.

$$v_o = \left(\frac{C_0^{1-n}}{t}\right)\ln\left(\frac{N_{T_1}}{N_{T_2}}\right)[\exp(-\Delta E/kT_1)-\exp(-\Delta E/kT_2)] \qquad (7\text{-}1)$$

$$v_O = \left(\frac{C_O^{1-n}}{t}\right) \ln\left(\frac{N_O + N_{TO} - N_{T_1}}{N_O + N_{TO} - N_{T_2}}\right) [\exp(-\Delta E/kT_1) - \exp(-\Delta E/kT_2)] \quad (7\text{-}2)$$

The term representing the initial reactant concentration, C_o^{1-n}, must be assumed for a given value of n, which means that the derivation for v_o is not completely independent of the reaction order, n, and some iterative process is required to derive the order and the reaction velocity. At low implant doses, it is assumed that the relative change of entropy in a crystalline substrate is small as implant damage is removed because no phase change from crystalline to amorphous material occurs as a result of implant damage. Thus, the activation enthalpy may be assumed to be equal to the activation energy, ΔE.

The model described above remains powerful despite the requirement of an iterative process to separate the effects of the reaction velocity and the reaction order. By making use of this method, a user may derive the temperature and time dependence of a set of solid state reactions by observing the change in reactant and product concentrations over a series samples annealed at a constant time at a variety of temperatures ranging from “room temperature” to a user-specified limit. This has the potential for reducing a design space by a full order of magnitude in size. Naturally, the accuracy of this model is very dependent upon the degree to which the second term in the expression for the variation of the reactant concentration, as shown in (4-1) and (4-2), is less than one. To this end, it is advantageous to reduce the annealing time as well as the annealing temperature associated with the experiment to the smallest possible magnitudes. A general rule of thumb regarding the Taylor Expansions performed is that if the second term in the equation computes to a value of one tenth or less, the Taylor Expansion

should be accurate to approximately ten percent, making the approximation using this Taylor Expansion accurate enough for use in the derivation

4.2: Experimental Procedure

In order to verify the utility of the expressions developed below, isochronal annealing curves were developed for analysis. MOS Capacitors were fabricated in the fashion described in Section 3.2. They were fabricated on a P-type Si sample with a resistivity in the range of 8 Ω-cm to 15 Ω-cm with an average insulator thickness and standard deviation of 194.58 Å and 5.748 Å, respectively, over the surface of the sample. The sample was implanted with molecular hydrogen, H_2^+, at an energy of 20 keV, a tilt of 7 degrees, a rotation of 45 degrees and a variable fluence ranging from $1x10^{12}$ H_2/cm^2 to $1x10^{14}$ $H_2/cm^2$and were put through the same post-implant as was described in Section 3.2 with the exception of varying the annealing temperature. The annealing temperature for the samples being investigated varied from 300°C to 600°C.

These samples were labeled according to their implant species, dose and intended post-implant anneal status (that anneal status either being as-formed or annealed at 600°C for 30 minutes). Following analysis of those samples implanted with the varying H_2^+ dose, a second batch of both p-type samples were implanted with a fluence of $1x10^{13}$ H_2^+/cm^2 which was found to be the optimal dose to generate proper characteristics from DLTS in both. This dose demonstrated optimal operation in an as-formed state as well as when annealed at 600°C for 30 minutes. In the case of a selected dose of $1x10^{12}$ H_2^+/cm^2, poor DLTS characteristics of the annealed sample, likely caused by an insufficient Molecular Hydrogen dose to induce self-sintering of the Silicon-Oxide interface, precluded the use of a low-dose treatment for the

formation of DLTS samples. Conversely, in the case of a selected dose of $1x10^{14}$ H_2^+/cm^2, the poor DLTS characteristics of the as-formed sample, likely caused by excess insulator damage caused by the high implant fluence, precluded a high dose from use in DLTS treatments. New p-type samples implanted with H_2^+ at a fluence of $1x10^{13}$ H_2^+/cm^2 were annealed at temperatures varying from 300°C to 600°C at 100°C increments with one sample left over for analysis as an as-formed sample after implant. It was this last set of samples which would form the core of the proof of concept experiment for evaluation of Deep Level Trap annealing characteristics through the use of Kinetic Differential Analysis.

Control of the depth probed into the bulk was accomplished by assuming a constant doping between wafers and maintaining a constant surface potential during the filling and emission pulses from sample to sample. This was accomplished by defining the depletion capacitances necessary from sample to sample in terms of the constituent accumulation capacitance, which is simply the Oxide Capacitance, and the inversion capacitance, which is simply the depletion capacitance with the Surface Potential equal to twice the Fermi Potential, as well as the ratio (r) of the Surface Potential to twice the Fermi Potential. By noting that the depletion width depends on the inverse squared root of the ratio between the surface potential and the Fermi Potential and thus the depletion capacitance varies with the squared root of the ratio, the following expression may be derived for the effective capacitance observed for an MIS Capacitor with the depletion capacitance in series with the Oxide Capacitance.

$$C_{eff} = \frac{C_{inv} C_{ox}}{C_{ox}\sqrt{r} + C_{inv}(1-\sqrt{r})} \quad (8)$$

$$r = \frac{\varphi_S}{2\varphi_f} \quad (9)$$

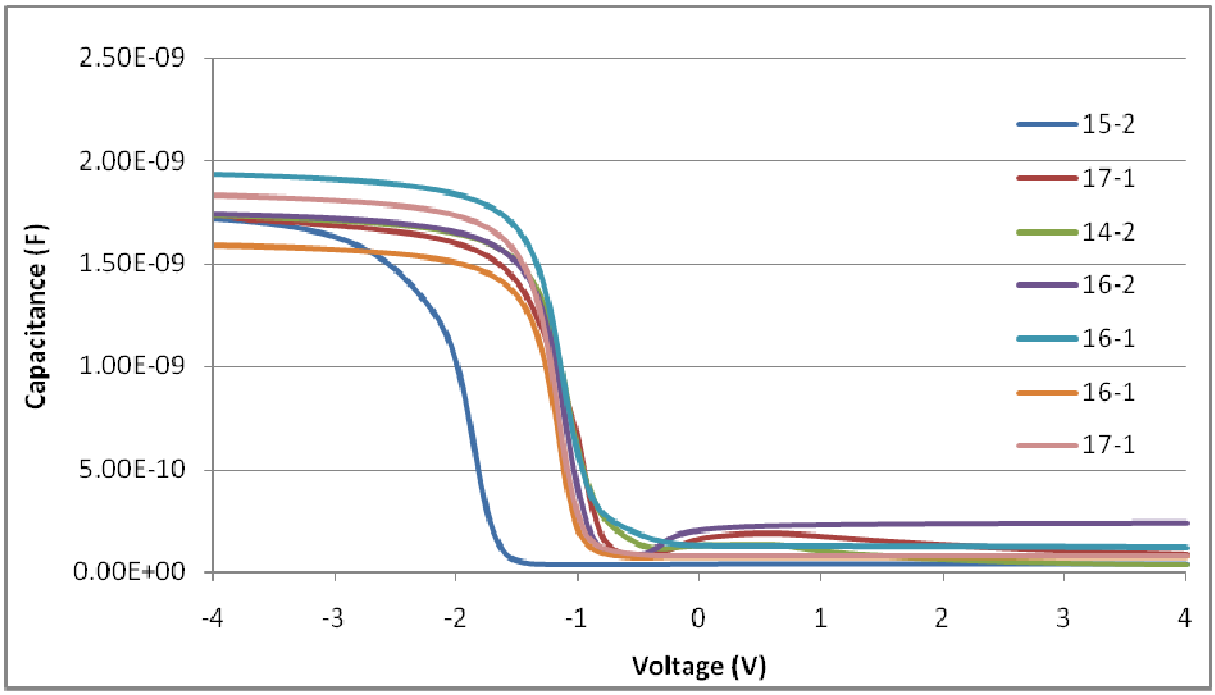

Figure 2: Capacitance Voltage data for DLTS MIS Capacitors – The observed shift in flatband voltages between the room temperature sample and annealed samples is assumed to be caused by ionized charges in the oxide caused by the ion implantation of hydrogen into the sample.

Samples were cooled to 100K and heated to 400K with measurements of the capacitance transient taken every 0.25K as heating occurred. These transients were analyzed using a boxcar integration technique with windows defined at $7t_D$ and $2.3t_D$ where t_D is equal to the machine-defined variable time delay ranging from 5ms to 0.1ms. The resulting spectra were analyzed assuming a single-exponential dependency via a combination of Arrhenius plotting and HWNM measurements. Kinetic Differential Analysis was performed on the resulting DLTS measurements by determining discrete differential rate of reaction between the as-formed sample

and samples annealed at variable temperatures. This differential was evaluated by comparing the magnitude of peak maxima from one sample to the next.

Sample	Anneal (°C)	Oxide Thk (A)	Oxide StDev (A)	Emission Pulse (V)	Filling Pulse (V)
15-2	Room	189	2	-1.65	-1.85
15-1	300	189	2	-0.75	-0.95
14-2	450	191	3	-0.5	-0.8
14-1	350	191	3	-0.85	-1.05
16-2	400	191	3	-0.6	-1.1
16-1	500	191	3	-0.9	-1.1
17-2	550	190	3	-0.7	-1
17-1	600	190	3	-0.85	-1.1

Table 1: Sample Preparation data for DLTS Samples – DLTS samples were annealed at varying temperatures after subjected to an oxidation. The average thickness and standard deviation of this thickness are tabulated above along with the applied emission pulse voltage and filling pulse voltage, which are tabulated with the sample ID.

Following the generation of DLTS MIS Capacitor samples as detailed above, four double polished bare 4-inch wafers with a p-type resistivity in the same range as the MIS samples were implanted by Core Systems Inc. on a rotary ion implanter at 20 KeV with a tilt of 7 degrees and a dose of $1x10^{16}$ H_2^+/cm^2. One sample was maintained as an as-formed sample while seven other samples were annealed for 30 minutes in a temperature of range of 300°C to 600°C with steps of 50°C. These double-polished samples were analyzed for structural defects using MIT-IR. MIT-IR measurements were performed on the implanted samples, both as-formed and annealed, between 2300 and 1800 cm^{-1} at quarter cm^{-1} increments. This measurement was also performed on a virgin double-polished baseline sample where no ion implantation step was performed. The infrared beam used for attenuation analysis was guided through a single crystal silicon prism with a 30μm groove etched in the center and with a bevel angle of 30°. The infrared beam was

directed perpendicular to the beveled edge so that the effective angle of transmission into the samples being analyzed was approximately 30°. The transmission signals from the implanted samples were divided by that of the baseline sample and the negation of the natural logarithm of the resulting ratio was taken to yield a series of MIT-IR spectra corresponding to observed defect density signals. Signals which demonstrated longevity over a broad temperature range were analyzed using Kinetic Differential Analysis by determining discrete differential rate of reaction between the as-formed sample and samples annealed at variable temperatures. This differential was evaluated by comparing the magnitude of peak maxima from one sample to the next.

4.3: Results and Discussion

Analysis of MIT-IR Spectroscopy data in the annealing temperature range of 300°C to 600°C and comparison of this data to an as-formed sample provided information regarding the annealing kinetics of defects formed by the Ion Implantation of hydrogen into silicon.

Species	Wavenumber (cm^{-1})
IH_X	1950,1960
VH_1	2025
VH_2	2127
VH_3	2180,2161
VH_4	2209

Table 2: A compilation of IHx and VHx vibrating mode absorption wavenumbers.

Six separate resonant states were observed during analysis. These signals included four resonant states corresponding to three separate decorated vacancy species and two resonant states corresponding to the decorated interstitial species, IH_2. The resonant states corresponding to IH_2 which demonstrated substantial activity through the annealing temperature range were those belonging to 1950 cm^{-1} and 1960 cm^{-1}. A single resonant state belonging to VH_2 was observed at 2127 cm^{-1}. Resonant states belonging to VH_3 at 2180 cm^{-1} and at 2161 cm^{-1} as well as a single resonant state belonging to VH4 at 2209 cm^{-1} were also observed.

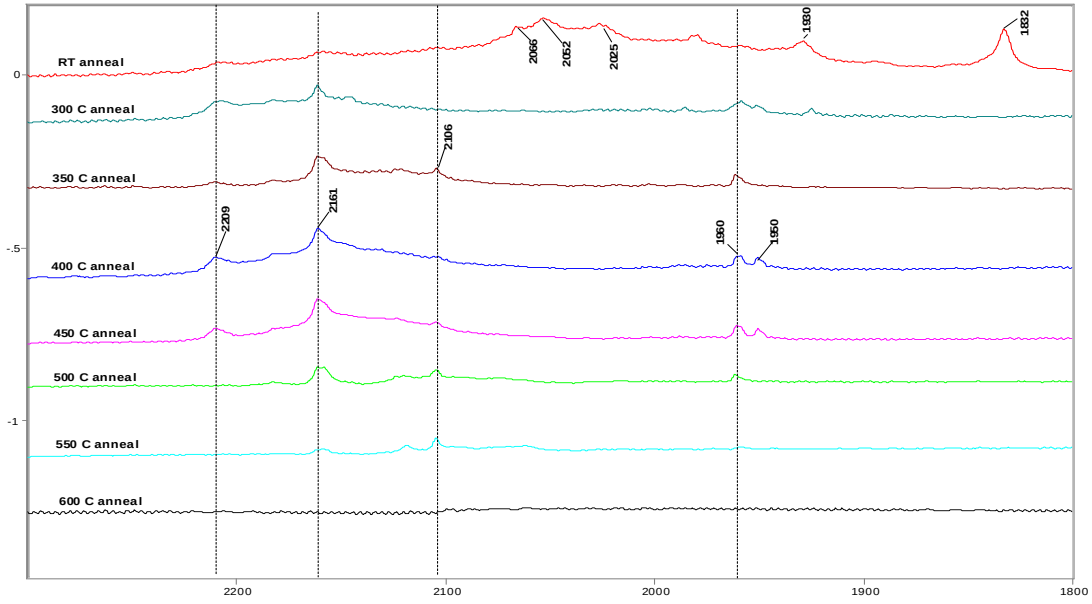

Figure 3: MIT-IR Spectroscopy Data (Courtesy: Greg Buchar Corning Incorporated) – This data was taken from Double Polished Si wafers annealed in a temperature range from room temperature to 600C. VH_x defects as well as IH_x defects were observed through the entire temperature range. Hydrogen bonded to internal <111> interfaces as well as trapped H_2 molecules were observed in the as-formed sample.

The magnitude of the MIT-IR signal, which itself is linearly related to the defect concentration within the ion implanted region, demonstrated that the decorated silicon interstitial defect, IH_2 decayed rapidly after its genesis during ion implantation. No evidence of a generation reaction at low temperatures was observed. As the decay of IH_2 proceeded out to 450°C, a generation reaction was observed at high temperatures which substantially slowed and even halted the rate of IH_2 decay in the 450°C to 550°C temperature range. The concentration for IH_2 in this regime was approximately 30% of the initial concentration observed in the as-formed sample. The decay of IH_2 resumed, approaching completion at 600°C, where a secondary decay reaction must have become dominant. This is a significant observation. IH_2 has been theorized to contribute catalytically to the reaction of oxygen in silicon during the formation thermal donors. If the decay of IH_2 may be slowed by a generation reaction at moderate temperatures between 450°C and 550°C, it may contribute substantially to the formation of additional thermal donors in this same temperature range, resulting in enhanced n-type behavior in annealed samples which might compensate or even invert the dominant carrier type of a sample, even at high temperatures.

Unlike the MIT-IR signals corresponding to IH_2, the MIT-IR signals corresponding to the decorated vacancy defects indicated the dominance of some generation reaction at low temperatures below 300°C, as the observed signal magnitudes associated with VH_2, VH_3 and VH_4 were higher for the sample annealed at 350°C than for the sample kept in an as-formed state, as shown in Figure 5 and Figure 6. This suggests that the efficiency of any heat sink which samples are affixed to during implantation as well as the associated temperature at which samples are implanted may contribute substantially to the enhancement or reduction of decorated monovacancies in samples implanted with hydrogen. A decay reaction dominated the annealing

kinetics in the temperature range of 350°C to 500°C, as shown in Figure 4. In the 500°C to 600°C range, this decay reaction was stalled temporarily by a secondary generation reaction. This reduction of the decay kinetic at elevated temperatures may be responsible for the enhanced p-type carrier concentrations observed in samples after annealing at elevated temperatures in the 500°C to 600°C range. Monovacancies decorated with over one hydrogen atom are generally considered to be acceptors. It should be noted that the relative reduction of the decay rate due to the generation reaction occurring at temperatures in excess of 500°C result in the maintenance of a constant concentration equal to approximately 15% of the as-formed concentration and, as such, are smaller than the secondary generation rate associated with IH_2, which is readily observable in Figure 7. In the case of the observed decay of the 2161 cm^{-1} peak associated with VH_3, this secondary generation reaction doesn't manifest itself at all.

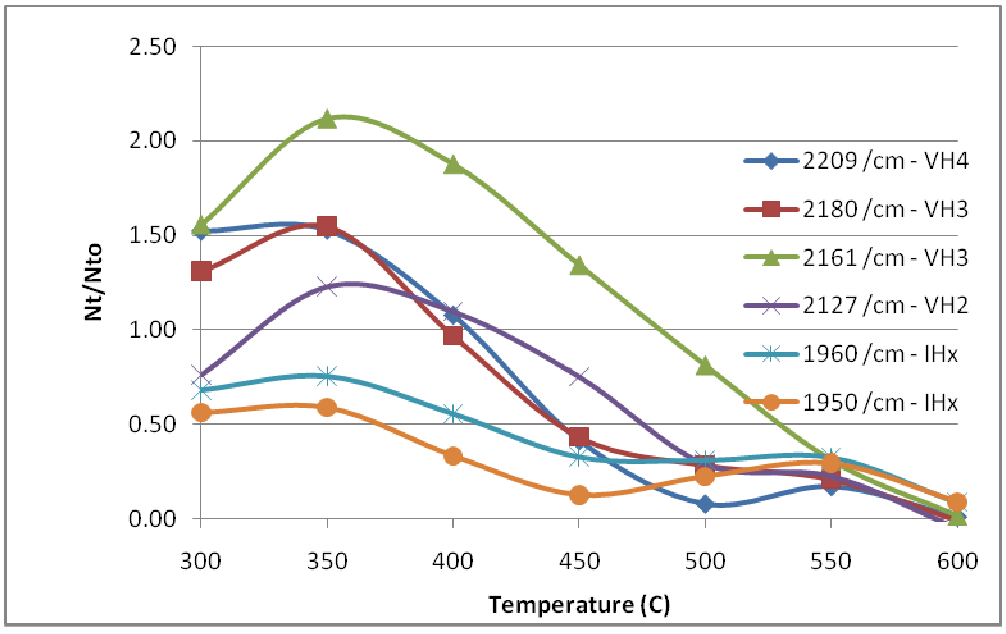

Figure 4: MIT-IR spectral intensities with respect to temperature – Evidence of some generation reaction at low temperatures is evident as well as a secondary generation reaction which slows decay at elevated temperatures. This is the case for all spectra, but is more readily apparent for decorated interstitials than for decorated vacancies.

The as-formed sample generated by ion implantation demonstrated a substantial number of additional peaks past the group listed above which manifested themselves as a band extending from 2066 cm^{-1} to 1931 cm^{-1} as well as a single peak at 1832 cm^{-1}. The band is comprised of a series of peaks representing hydrogen bonded to internal surfaces as well as denuded internal surfaces while the peak at 1832 cm^{-1} represented molecular hydrogen trapped by internal surfaces. The observable peaks within the band at 2052cm^{-1} as well as 2066cm^{-1} represented hydrogen bonded to the internal surfaces of a (111) dislocation loop while the peak at 2025cm^{-1} represented the VH monovacancy defect. This defect anneals out at a surprisingly low temperature; all but disappearing after a 30 minute anneal at 300°C is performed. It is likely that this defect along with the dissociation of the (111) dislocation loops, which also decay fully by 400C, contribute to the substantial generation of monovacancy defects decorated with more than one hydrogen atom.

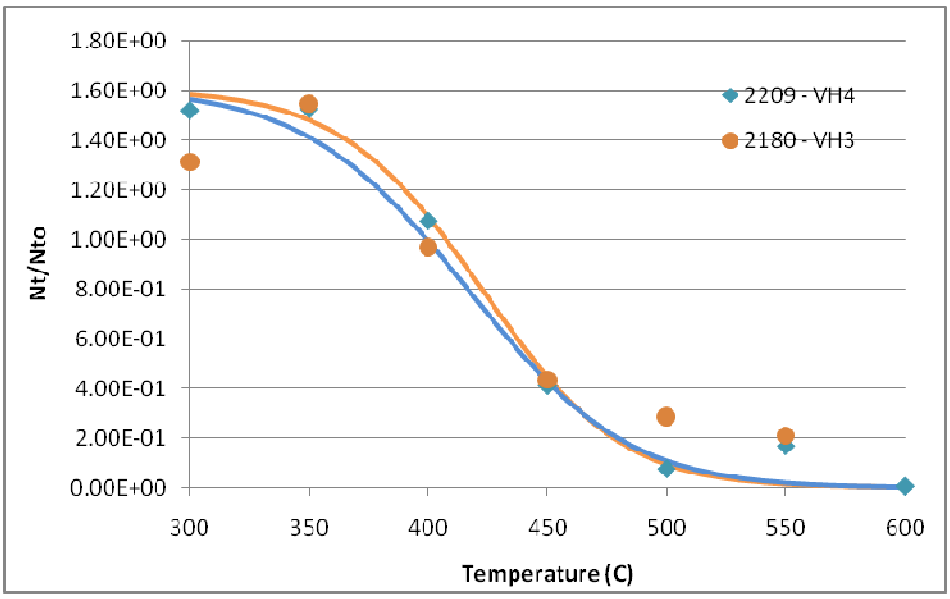

Figure 5: Fitted and Normalized Data for 2209 cm^{-1} and 2180 cm^{-1} – This data indicates that a weak secondary generation reaction is occurring, and that a reaction order of approximately 1.5 yields a reasonable fit to the decay reaction data.

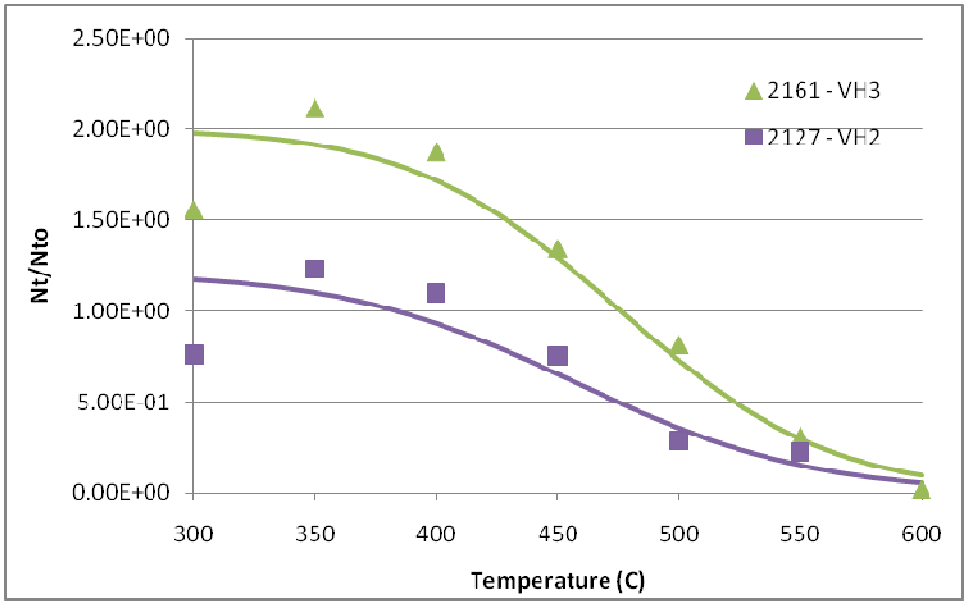

Figure 6: Fitted and Normalized Data for 2161 cm^{-1} and 2127 cm^{-1} – The presence of a secondary generation reaction is not suggested out by this data. A reaction order of approximately 1.5 yields a reasonable fit to the decay reaction data.

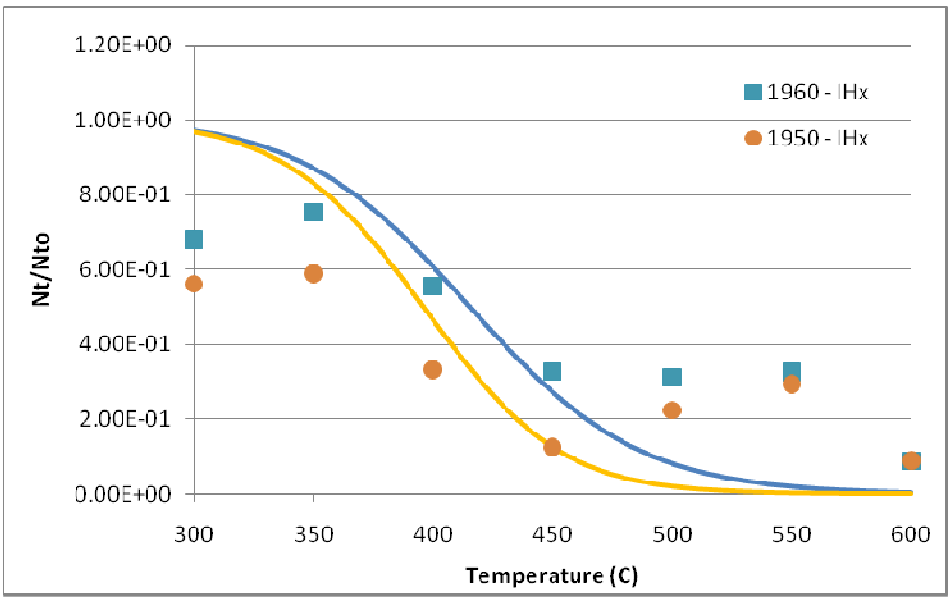

Figure 7: Fitted and Normalized Data for 1950 cm^{-1} and 1960 cm^{-1} – The presence is readily evident in this data. A reaction order of approximately 1.5 yields a reasonable fit to the decay reaction data.

Differential analysis of the variations in defect concentration with respect to annealing temperature were made possible by redefining the equations corresponding to analysis of a decay reaction by normalizing to the maximum concentration and treating it as though it were the initial concentration. This maximum occurred at 350°C for all trap species. This alteration roughly corresponds to an assumption that any generation reaction possesses an activation energy barrier that is sufficiently small that the reaction occurs much more rapidly than the decay reaction at the temperatures at which the decay reaction begins to dominate the kinetics. The generation reaction will have already run to completion by the time the decay reaction begins to eliminate defects. It should be noted that this assumption is not an accurate one for situations where the decay reaction results in species which are reactants in the generation reaction. After normalization to the curve maximum, the reaction order was determined iteratively by varying n, calculating the resulting activation energy and thermal velocity from the experimental curve and

observing the squared error between a generated curve and the experimental curve. The case for determining the reaction order was the point at which the squared error between the generated theoretical curve and the experimental curve was minimized. This error was only considered along the points analyzed to determine the activation energy and reaction velocity so as to avoid any convolution with high temperature generation reactions which would skew the reaction curve to lower activation energies and reaction velocities. The "second term" used to evaluate the validity of the Taylor Expansion used in deriving both the activation energy and the reaction velocity was maintained at a value below two tenths. This could generally be accomplished by avoiding any points along the annealing curve there the value of C/Co strayed below four tenths.

Analysis of the temperature response of the reaction differential was complicated by the coarse granularity of the measurement with respect to temperature. In some cases, only two separate points on the decay curve could be used to calculate the activation energy, yielding a single measurement of the activation energy from which the behavior of the annealing curve had to be derived. This error likely contributed to errors in the reaction velocity, as well. Despite the threat of significant errors, theoretical reaction curves were generated which fit closely with experimental data. It may be assumed that this fit would be improved and the errors associated with reaction velocity, activation energy and reaction order extraction could be greatly reduced by moving to a finer temperature granularity in the measurement.

	2209	2180	2161	2127	1950	1960
n (-)	1.50	1.45	1.44	1.41	1.55	1.48
ΔH (eV)	1.21	1.02	0.94	0.80	0.69	1.14
vo (s^{-1})	$4.86x10^{8}$	$2.09x10^{7}$	$1.53x10^{6}$	$1.98x10^{5}$	$8.21x10^{4}$	$2.81x10^{8}$

Table 3: Extracted Reaction Coefficients for IR Spectra – This data indicates a common reaction order of roughly 1.5. The activation enthalpy of the decay reaction appears to increase with increasing defect decoration for monovacancy defects.

Analysis of the primary decay reaction observed in the MIT-IR studies indicated a reaction which is likely self-catalyzing, with a reaction order around 1.5. This indicates that the reaction is not simply brought about by the dissociation of defect species. Nor is it brought about by the collision of hydrogen with observed defect species. There exists some interaction between defect species associated with the reaction. Another interesting energetic characteristic associated with the reactions observed with MIT-IR is the increase in activation energy associated with decay as "decoration" increases. As monovacanies gain additional hydrogen atoms, they transition from activation energy of approximately .8eV for VH_2 to an approximate activation energy of 1eV for VH_3 to an activation energy of 1.2eV for VH_4. If this effect proves to be statistically significant, it indicates that the likely pathway for reaction is not dissociation of decorated molecules followed by the recombination of undecorated Frenkel Pairs. Rather, the reaction pathway is the increased decoration of monovacancies. VH becomes VH_2 which becomes VH_3 which yields VH_4 which combines with other VH_4 molecules to create decorated multivacancies. As the "decoration" of the monovacancy species increases, the interaction between bonded hydrogen atoms increases and the energy required to force an additional atom into the defect site and promote the monovacancy up to the next most defective site increases, which accounts for the trend of increasing activation energy with increasing "decoration".

An additional noteworthy characteristic is the similarity in reaction order for the dual peaks associated with VH_3 (around 1.45) but differing dissociation energies. If this deviation in dissociation energy is statistically significant, this may be an indicator that the two peaks generated for VH_3 correspond to different molecular coordinations where one molecular coordination is more permissive of further decoration to form VH_4 than the other molecular coordination.

Trap	Species	ΔE (eV)	ΔE Max	ΔE Min	σ (cm^3)	σ Max	σ Min
H1	VH2?	0.149	0.153	0.146	$7.37x10^{-17}$	$1.07x10^{-16}$	$5.07x10^{-17}$
V1	V++	0.118	0.134	0.101	$5.56x10^{-17}$	$4.21x10^{-16}$	$7.02x10^{-18}$
H2	VH3?	0.161	0.168	0.154	$2.55x10^{-18}$	$4.40x10^{-18}$	$1.48x10^{-18}$
H3	IHx?	0.186	0.194	0.178	$8.41x10^{-18}$	$1.52x10^{-17}$	$4.67x10^{-18}$
V2	VV	0.228	0.233	0.223	$4.49x10^{-19}$	$5.72x10^{-19}$	$3.52x10^{-19}$
F1	Bi-Hi	0.552	0.563	0.541	$4.40x10^{-15}$	$6.78x10^{-15}$	$2.86x10^{-15}$
F2	Bi-Hi	0.539	0.549	0.529	$4.55x10^{-16}$	$6.49x10^{-16}$	$3.19x10^{-16}$
C1	Ci-Oi	0.378	0.388	0.368	$8.54x10^{-16}$	$1.44x10^{-15}$	$5.05x10^{-16}$
B1	Ci-Oi	0.303	0.342	0.263	$4.28x10^{-15}$	$6.06x10^{-14}$	$3.02x10^{-16}$
B2	??	0.664	0.714	0.614	$1.18x10^{-10}$	$1.24x10^{-09}$	$1.12x10^{-11}$

Table 4: Observed trap species – Variable trap species were observed from 300C to 600C. These trap species included monovacancies and bonded double-vacancies, interstitial carbon-oxygen bonds, interstitial boron hydrogen bonds and defects attributed to decorated monovacancies and interstitials.

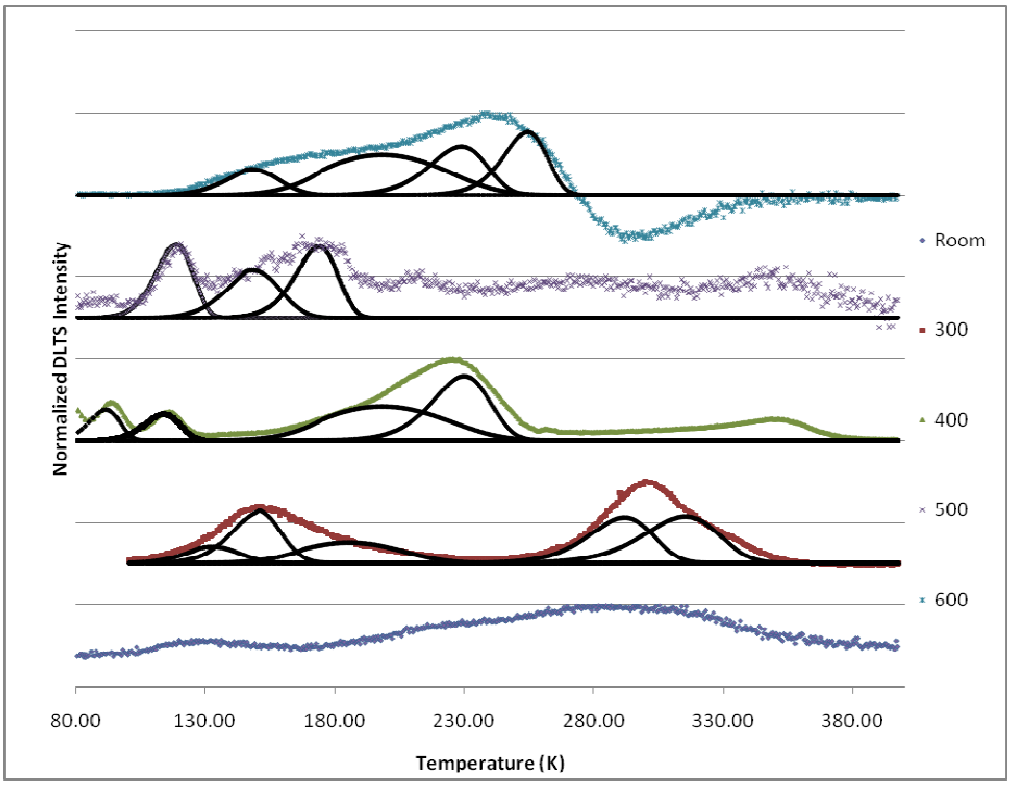

Figure 8: Normalized DLTS Intensity Data – Data ranging from the as-formed state to a state corresponding to an anneal performed at 600°C is included. Additionally, the de-superposition of each DLTS peak and the resulting contributing spectra are included.

The large band of defects observed during MIT-IR measurements of the as-formed sample is also observed during DLTS measurements. In total, ten separate defects contributed to this observed band. Of these ten defects, two manifested themselves at traps at energies of .38eV and .33eV above the valence band and capture cross sections of 4.3×10^{-15} cm^2 and 8.5×10^{-16} cm^2, which put them in the cryogenic temperature range associated with interstitial carbon-carbon bonds. Assuming that this defect is the same as the defect described in literature as corresponding to the VH_2 defect, it may be reasonably stated that the fit which yielded this result in literature was to a carbon-carbon bond, not to the VH_2 defect. Of these two defects, the defect at .33eV demonstrated a very poor fit with a standard deviation of nearly 30meV. In

comparison, the defect at .38eV demonstrated a much better fit with a standard deviation of approximately 10meV. The likely cause of this discrepancy is due to the noisy quality of the DLTS spectrum at which the .33eV peak signal was observed as a distinct peak. An additional peak was observed at .23eV above the valence band with a capture cross section of $4.5x10^{-19}$ cm^2, putting it in the same cryogenic temperature range as the divacancy. At the shallow end of the DLTS spectra, an additional peak was observed in the DLTS spectrum at an energy of .13eV relation to the valence in band and with a capture cross-section of $5.6x10^{-19}$ cm^2, correlating it with the double-positive vacancy defect. These two defects were fitted well with standard deviations of approximately 10meV, further illustrating the power available when the Half Width at "N^{th}" Maximum is used for data extraction.

Two separate families of peaks were observed which could not be correlated with bombardment-induced defects observed by DLTS or EPR. The first family of these defects was present at high cryogenic temperatures and high energies above the valence band, manifesting themselves as a peak and corresponding shoulder at 300C. They had energies of .55eV and .54eV and capture cross sections of $4.5x10^{-15}$ cm^2 and $4.5x10^{-16}$ cm^2, demonstrating a strong fit with a standard deviation of approximately 10meV. These defects would, typically, be correlated with an interstitial Boron-Hydrogen bond, as was discussed previously in section 1.5.

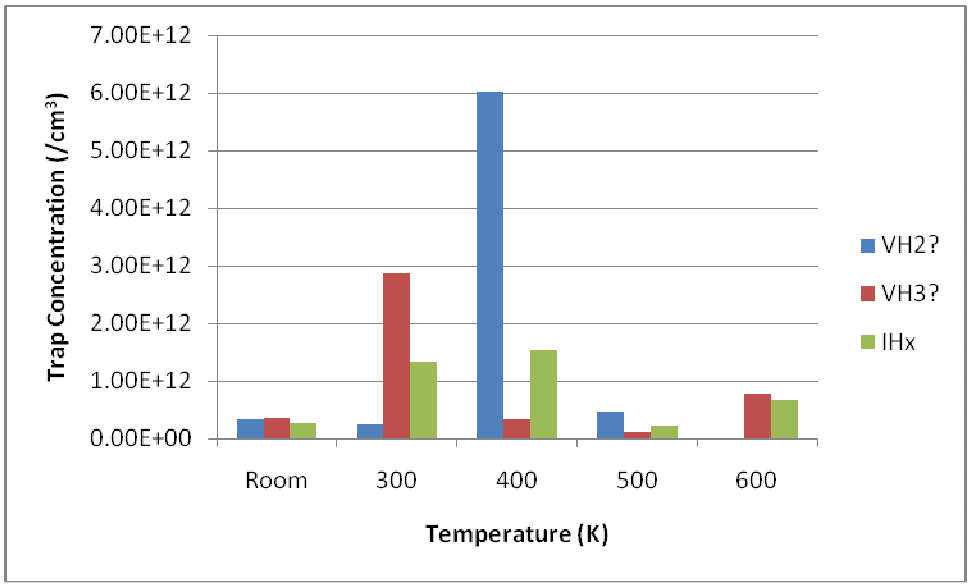

Figure 9: Temperature Dependance of Hydrogenated Defects – Defects attributed to decorated vacancies and interstitials appear to peak in concentration in the 300°C to 400°C range, an observation consistent with MIT-IR spectra. A substantial secondary generation reaction appears evident for IHx, consistent with MIT-IR data.

It is assumed that the two shallowest energy levels at .15eV and .16eV and the deep level at approximately .186eV represented two separate families of peaks. In the case of hydrogen decorated monovacancies, the general assumption is made that defects with the largest energy difference between the valence band at the defect energy correspond to the defect with the most hydrogen atoms bonded to them. Furthermore, the defect with full hydrogen bonding, VH_4, may be considered electronically inert. Utilizing this assumption, the .15eV peak corresponds to the VH_2 defect while the .16eV peak corresponds to the VH_3 defect. The defect at .186eV is assigned to IHx defects because of its relatively high concentration even at 600°C, which closely fits the infrared behavior of the observed IHx defects.

It should be noted that one additional energy signature was observed at approximately .66eV above the valence band. However, the observed peak had a very poor fit, with a standard

deviation of nearly 100meV and also possessed a very large capture cross-section of $1x10^{-10}$ cm^2. This energy is similar to the energy observed and correlated with the VH_3 defect in literature. It should be noted that the annealing behavior of this defect does not match well with MIT-IR Spectra for VH_3 and, because of this, the correlation between this energy level and VH_3 should be called into question.

Chapter 5: Conclusion

1.1: Analytical Methods

Theoretical analysis of the transient characteristics and the associated DLTS response of an MIS capacitor have demonstrated that raising the insulator capacitance increases the ratio of bulk DLTS signals to interface state signals. Furthermore, an expression for the DLTS signal of an MIS capacitor in terms of the oxide capacitance and depletion capacitance has been derived. The effects of large interface state densities and the distortion of the DLTS signal associated with their emission have been demonstrated. As a result of this analysis, a sample fabrication technique was established whereupon an oxide with a thickness of around 20 nm was grown and ions were ballistically injected at low fluencies through the oxide into the semiconductor to populate it with ion damage which could then be analyzed using DLTS.

A new method of analyzing DLTS signals has been developed. This is the Half Width at "N^{th}" Maximum, where N is the ratio between the magnitude of the DLTS signal along the side of the peak and the magnitude of the peak maximum. This method relates the width of a DLTS peak to the energy difference between the trap energy and the band associated with majority carrier emission through the use of a scaling constant, k_o, which is related to the machine settings of the DLTS electronics and the ratio, N. The position of the DLTS maximum with respect to temperature defines the capture cross section. This represents a much more efficient and accurate method for determining capture cross section and trap energy in comparison to Arrhenius fitting which requires substantial investments in terms of time and capital and which is also very prone to distortion effects.

A novel method for the analysis of solid state chemical reactions has been derived. This methodology is termed "Kinetic Differential Analysis" and may be utilized to substantially reduce the design space required for analysis of solid state reaction kinetics. By comparing the concentration of products and reactants in a sample annealed at a variable temperature and constant time to an as-formed sample, the activation energy, reaction velocity and reaction order may be determined.

Lastly, a formula has been developed detailing the attenuation effects associated with MIT-IR measurements both generated by means of guiding through a silicon prism into a double-polished silicon wafer. Analysis led to the development of a function relating the attenuation generated purely by ion implant damage to the ratio of the difference between signals generated from a non-implanted baseline sample and from an ion implanted sample populated with significant implant damage. A method for deriving the optical capture cross-section by correlating the magnitude of an MIT-IR peak to the observed trap density of a corresponding DLTS peak has also been outlined.

1.2: Ion Implant Related Defects

Analysis of H_2^+ ion implanted defects via MIT-IR has identified the reaction kinetics of decorated monovacancies as well as decorated interstitials. In general, monovacancy reactions are characterized by a low-temperature generation reaction which gives way to a mid-temperature decay reaction which brings about the decay of the majority of the monovacancy concentration. This mid-temperature reaction is characterized by a reaction order of approximately 1.5, which indicates that some reactant interaction must be taking place during

decay. This indicates that decorated monovacancies cannot simply shed hydrogen atoms or pick up additional hydrogen atoms in a reaction. Furthermore, analysis of activation energies indicates that the activation energy of the mid-temperature decay reaction appears to increase with increasing decoration. The statistical significance of this trend has not yet been ascertained; however data suggests a correlation between decoration and effective binding energy. The mid-temperature decay is impeded at high temperatures by a secondary generation reaction which preserves substantial concentrations of decorated monovacancy defects.

Decorated interstitials do not follow the same reaction trend. They are not subject to the same low-temperature generation reaction as the decorated monovacancies and the high-temperature generation reaction which they do undergo is much more effective in impeding the mid-temperature decay reaction.

Analysis of DLTS spectra identified peaks corresponding to carbon-oxygen interstitials, bonded divacancy defects monovacancies and boron-hydrogen interstitial complexes. Amongst the defects identified, three defects, corresponding to trap energies of .15eV, .16eV and .19eV above the valence band were assigned to VH_2, VH_3 and IH_x defects, respectively.

	VH4	VH3	VH2	IHx(1)	IHx(2)
ΔE (eV)	-	0.16	0.15	0.19	0.19
σ (cm3)	-	$2.55x10^{-18}$	$7.37x10^{-17}$	$8.41x10^{-18}$	$8.41x10^{-18}$
n (-)	1.50	1.45	1.41	1.55	1.48
ΔH (eV)	1.21	0.98	0.80	0.69	1.14
vo (/s)	$4.86x10^{8}$	$1.12x10^{7}$	$1.98x10^{5}$	$8.21x10^{4}$	$2.81x10^{8}$

Table 1: Trap Energies, Capture Cross Sections, Reaction Orders, Reaction Energies and Reaction Velocities of identified H_2^+ ion implant defects.

1.3: Future Work

The development of the analytical techniques introduced in this text has paved the way for a detailed study of the reaction kinetics of electronic defects and their corresponding physical defects via DLTS and MIT-IR studies. Future analysis of reaction kinetics at low temperatures will be of likely interest because of their contribution to formation kinetics in ion implantation techniques where the substrate is thermally insulated during ion implantation. A re-analysis of mid-temperature and high-temperature annealing kinetics must be performed with much tighter constraints on measurement granularity with respect to temperature, both in MIT-IR and DLTS measurements. This would allow for identification of activation energies and reaction velocities with a much higher level of confidence.

Work has already begun on analysis of TFTs fabricated at RIT with Deep Level Transient Spectroscopy. In this case, analysis would be performed via current DLTS measurements. This new method of analysis will make use of HWNM fitting methods. Studies of MIS Capacitors formed on SOI structures are also of profound interest. It is likely that the annealing characteristics of decorated vacancies and interstitials are dramatically influenced by the dissociation of denuded vacancies and interstitials. This dissociation is limited by diffusion in a bulk material. In a thin film material, such as SOI, this dissociation may be limited by both defect transport and surface recombination, resulting in an inherently lower rate in comparison to bulk diffusion.

Bibliography

1- A. Aspar, M. Bruel, H. Moriceau, C. Maleville, T. Poumeyrol, A.M. Papon, "Basic Processes Involved in the Smart Cut Process", Microelectronic Engineering **36**, 233-240 (1999).

2- M.K. Weldon, V.E. Mariso, Y.J Chabal, A. Agarwal, D.J. Eaglesham, J. Sapjeta, W.L. Brown, D.C. Jacobson, Y. Caudano, S.B. Christman, E.E. Chaban, "On The Mechanism of Hydrogen Induced Exfoliation in Silicon", J. Vac. Sci. Technol. B **15**, 1066 (1997).

3- F.D. Auret, P.N.K. Deenapanray, "Deep Level Transient Spectoscopy of High Energy Light Particle Irradiated Si", Crit. Rev. in Solid States and Mat. Sci. (2004).

4- D.V. Lang, "Deep Level Transient Spectroscopy: A New Method to Characterize Traps in Semiconductors", J. App. Phys. **45** No. 7, 3023-3033 (1974).

5- M.K. Weldon, V.E. Mariso, Y.J. Chabal, D.R. Hamann, S.B. Christman, E.E. Chaban, "Infrared Spectroscopy as a Probe of Fundamental Processes in Microelectronics: Silicon Wafer Cleaning and Bonding", Surface Science **368**, 163 (1996).

6- W. Shockley, "Electrons Holes and Traps in Semiconductors", Proc. IRE **46**, pp. 973-990, (1958).

7- E. Hecht, "Optics", Addison-Wesley, San Francisco, 112 (2002).

8- E. Hecht, "Optics", Addison-Wesley, San Francisco, 114 (2002).

9- B.D. Cullity, S.R. Stock, "Elements of X-Ray Diffraction", Prentice Hall, New Jersey, 153 (2001)

10- Y.J. Chabal, M.K. Weldon, Y. Caudano, B.B. Stefanov, K. Raghavachari, "Spectroscopic Studies of H-Decorated Interstitials and Vacancies in Thin Film Exfoliation" Physica B **273**, 152 (2000).

11- K. Bonde Nielsen, L. Dobaczewski, K. Goscinski, R. Bendsen, O. Andersen, B. Bech Nielsen, "Deep Levels of Vacancy Hydrogen Centers Studied with Laplace DLTS", Physica B **273**, 167 (1999).

12- O. Felisova, N. Yarykin, Eu. Yakimov, J. Weber, "Hydrogen Interaction with Defects in Electron Irradiated Silicon", Physica B **273**, 243 (1999).

13- S. Fatima, C. Jagadish, J. Lalita, B.G. Svenson, A. Hallen, "Hydrogen Interaction with Implantation Induced Point Defects in P-Type Silicon", J. Appl. Phys. **35**, 5630 (1999).

14- M. Bruni, D. Bisero, R. Tonini, G. Ottaviani, G. Queirolo, R. Bottini, "Electrical Studies on H Implanted Silicon", Phys. Rev. B **49** 5291 (1994).

15- L.C. Kimerling, "New Developments in Defect Studies in Semiconductors", IEEE Trans. Nucl. Sci. **NS-23** 6 (1976).

16- L. W. Song, X.D. Zhan, B.W. Benson, G.D. Watkins, "Bistable Substitutional Carbon Interstitial Carbon Pair in Silicon" Phys. Rev. B **42** ,5762 (1990).

17- G.E. Jellison Jr., “Capacitance Transient Studies of an Electron Trap at EC-ET=.105eV in Phosphorus Doped Silicon” J. Appl. Phys. **53**, 5715 (1982).
18- P.M. Mooney, L. J. Cheng, M. Suli, J.D. Gerson, J.W. Corbett, “Defect Energy Levels in Boron Doped Silicon Irradiated with 1-MeV Electrons”, Phys. Rev. B **15**, 3836 (1977).
19- N.M Johnson, D.J. Bartelink, J.P. McVittie, “Measurement of Interface Defect States at Oxidized Silicon Surfaces by Constant Capacitance DLTS”, J. Vac. Sci. Technol. **16**, 1407 (1979).
20- R.F. Pierret, “Semiconductor Device Fundamentals”, Addison-Wesley, San Francisco, 578 (1996).
21- F. Murray, R. Carin, P. Bogdanski, “Determination of High Density Interface State Parameters in Metal-Insulator- Semiconductor Structures by Deep Level Transient Spectroscopy”, J. Appl. Phys. **60**, 3592 (1986).
22- B.G. Streetman, S. Banerjee, “Solid State Electronic Devices”, Prentice-Hall, New Jersey, 265 (2000).
23- B.G. Streetman, S. Banerjee, “Solid State Electronic Devices”, Prentice-Hall, New Jersey, 275 (2000).
24- R.F. Pierret, “Semiconductor Device Fundamentals”, Addison-Wesley, San Francisco, 584 (1996).
25- D.K. Schroeder, “Semiconductor Materials and Device Characterization”, Wiley-IEEE Press, New Jersey, 259 (2006).
26- K.L. Wang, “MOS Interface State Density Measurements Using Transient Capacitance Spectroscopy”, IEEE Trans. Electron Devices **27** Vol. 17, 2231 (1980).
27- D.V. Lang, “Space Charge Spectroscopy in Semiconductors”, Topics in Applied Physics **37**, 118.
28- J. Lauwaert, J. Van Gheluwe, P. Clauws, “An Accurate Analytical Approximation to the Capacitance Transient Amplitude in Deep Level Transient Spectroscopy for Fitting Carrier Capture Data”, Rev. Sci. Instruments **79,** 093902 (2008).
29- D. Pons, “Accurate Determination of Free Carrier Capture Kinetics of Deep Traps by Space Charge Methods”, J. Appl. Phys. **55**, 3644 (1984).
30- A. Frost, R.G. Pearson, “Kinetics and Mechanism”, Wiley, New York, 9 (1954).
31- A. Frost, R.G. Pearson, “Kinetics and Mechanism”, Wiley, New York, 37 (1954).
32- H. Callen, “Thermodynamics and an Introduction to Thermostatistics”, Wiley, New York, 181 (1985). `